Author Manuscript

Author Manuscript

Author Manuscript

Author Manuscript

HHS Public Access

Author manuscript

Nature. Author manuscript; available in PMC 2023 May 25.

Published in final edited form as:

Nature. 2022 April ; 604(7904): 98–103. doi:10.1038/s41586-022-04560-0.

A stable hippocampal code in freely flying bats

William A. Liberti III[1,3], **Tobias A. Schmid**[2,3], **Angelo Forli**[1], **Madeleine Snyder**[1], **Michael M. Yartsev**[1,2]

[1]Department of Bioengineering, UC Berkeley, Berkeley, CA, USA.

[2]Helen Wills Neuroscience Institute, UC Berkeley, Berkeley, CA, USA.

[3]These authors contributed equally: William A. Liberti III, Tobias A. Schmid.

Abstract

Neural activity in the hippocampus is known to reflect how animals move through an environment[1,2]. Although navigational behaviour may show considerable stability[3–6], the tuning stability of individual hippocampal neurons remains unclear[7–12]. Here we used wireless calcium imaging to longitudinally monitor the activity of dorsal CA1 hippocampal neurons in freely flying bats performing highly reproducible flights in a familiar environment. We find that both the participation and the spatial selectivity of most neurons remain stable over days and weeks. We also find that apparent changes in tuning can be largely attributed to variations in the flight behaviour of the bats. Finally, we show that bats navigating in the same environment under different room lighting conditions (lights on versus lights off) exhibit substantial changes in flight behaviour that can give the illusion of neuronal instability. However, when similar flight paths are compared across conditions, the stability of the hippocampal code persists. Taken together, we show that the underlying hippocampal code is highly stable over days and across contexts if behaviour is taken into account.

Neural activity in the hippocampus is believed to support spatial memory and navigation across a wide range of species[1,2,13–15], including in bats[16,17]. Egyptian fruit bats (*Rousettus aegyptiacus*) possess exceptional spatial memory and are thought to rely on a cognitive map for goal-directed navigation[3,5,6,15,18,19]. Members of this species navigate along structured paths night after night for months, pointing to the potential existence of a stable representation of their environment[5,6]. Early studies using extracellular electrophysiological recordings in rats reported that the spatial firing of hippocampal neurons remained stable

Correspondence and requests for materials should be addressed to Michael M. Yartsev. myartsev@berkeley.edu.

Author contributions T.A.S., W.A.L. and M.M.Y. designed the research. W.A.L., T.A.S. and M.M.Y. analysed the data. T.A.S. performed experiments with help from W.A.L, A.F and M.S. Illustrations were made by M.S. The manuscript was written by W.A.L., T.A.S. and M.M.Y. with input from A.F. and M.S.

Competing interests The authors declare no competing interests.

Additional information

Supplementary information The online version contains supplementary material available at https://doi.org/10.1038/s41586-022-04560-0.

Peer review information *Nature* thanks Roddy Grieves, Torkel Hafting and the other, anonymous, reviewer(s) for their contribution to the peer review of this work.

Reprints and permissions information is available at http://www.nature.com/reprints.

Author Manuscript Author Manuscript Author Manuscript Author Manuscript

in familiar environments over days[10,20] and weeks[11], thereby supporting the existence of a stable hippocampal code[15]. By contrast, studies in mice using recent advances in optical imaging methods, which overcome several of the shortcomings associated with longitudinal monitoring of the activity of individual neurons using electrophysiological recordings[21,22], reported a highly dynamic code[7–9,12,23,24]. These studies found that, even in familiar environments, only a subset of hippocampal neurons remained spatially selective from one day to the next, yet the ones that did, maintained their original spatial preference, suggesting a temporally drifting positional code[7–9,12,23,24]. Thus, the stability of the hippocampal code in familiar environments and across species remains unclear.

Wireless imaging from hippocampus of flying bats

Here we used custom wireless miniature microscopes[25] to longitudinally image neural activity from the dorsal CA1 hippocampal region of Egyptian fruit bats (Fig. 1a–e and Methods) engaged in self-paced, goal-directed aerial foraging[26] (Fig. 1d and Extended Data Fig. 1). We expressed Ca^{2+} indicators (GCaMP6f) in CA1 neurons and monitored their activity through an implanted GRIN lens (Fig. 1b and Methods). This approach enabled us to track the activity of the same cells over multiple days (Fig. 1c). Consistent with previous electrophysiological recordings from the hippocampus of freely flying bats[16,17,27], we found that individual neurons were primarily active during flight (Fig. 1e), exhibited spatial selectivity (Extended Data Fig. 2a) and, combined, spanned the available environment (Extended Data Fig. 2b, c). Each bat ($n = 7$) developed a unique set of structured flight paths that were executed with high precision (Fig. 1f and Extended Data Fig. 3a, b). Aligning neural activity to specific flight paths revealed time-locked responses in the majority of recorded neurons (494 out of 562, or 87.9%, of regions of interest (ROIs) significantly tuned to flight; Fig. 1g, Extended Data Fig. 3c, d and Methods). Furthermore, neural activity was largely distinct for different flight paths, with spatially overlapping portions exhibiting more similar activity (Extended Data Fig. 4) irrespective of distance or angle to goal location (Extended Data Fig. 5) (but see ref. [28]).

Stable hippocampal tuning during flight

Flights along the same path were highly correlated both within and across days (the mean flight correlation changed at a rate of −0.001 per day, $R^2 = 0.68$, $P = 1.6 \times 10^{-3}$; Fig. 2a and Methods). As hippocampal activity is known to be modulated by ongoing spatial movement[29–31], including in bats[16,17,32], we leveraged the highly structured, stable nature of the bat's flight to assess hippocampal tuning stability during a spatial behaviour that exhibited low variability. We observed that spatial tuning was stable for the majority of neurons that were tracked over days (Fig. 2b–d, Extended Data Fig. 6a–h and Methods). Stability persisted even when specific paths had not been flown for several days, suggesting that stable spatial tuning may not require continuous behavioural reinforcement (Extended Data Fig. 6i, j). Only a small fraction of well-isolated ROIs (2.6%) that were clearly visible during one session could not be located during an adjacent session (Extended Data Fig. 7 and Methods).

Despite the overall stability exhibited by the majority of hippocampal neurons in flying bats, there was still a quantifiable decrease in the average tuning over days relative to repeated

Author Manuscript Author Manuscript Author Manuscript Author Manuscript

flight paths (significant linear decrease in mean ROI tuning correlation of 0.02 per day, $R^2 = 0.54$, $P = 9.1 \times 10^{-3}$; Fig. 2b; two examples are shown in Fig. 3a). However, we found that even these relatively small changes in tuning were significantly correlated with flight-to-flight variability (Fig. 3a–c, Extended Data Fig. 8a, b and Methods). For neurons tuned to multiple flight paths, we found that neural activity on more variable paths displayed greater variability ($P = 9.7 \times 10^{-15}$, Wilcoxon rank-sum test; Fig. 3d). Similarly, tuning stability was degraded when only considering unstructured flights (that is, unique flight paths that do not repeat and are therefore inherently more variable) compared with the bat's structured flights (Extended Data Fig. 8c and Methods), suggesting that stability is not an intrinsic property of individual neurons but instead reflects behavioural variance. To further understand how behavioural changes over days affect our estimation of neural tuning, we implemented a simulation in which stable spatial firing fields are convolved with the empirically observed flight paths. This enabled us to approximate a null model of a stable code that considers differences in flight patterns from day to day (Fig. 3e and Methods). We found that the empirically observed decrease in coding stability qualitatively matched what we would expect given behavioural drift and a stable underlying neural code (Fig. 3f).

Stable tuning across sensory contexts

The results presented thus far demonstrate that the hippocampal code in flying bats is highly stable, and the ability to estimate neural tuning stability can be compromised by variability in spatial behaviour. This in turn suggests that greater apparent tuning instability may arise from more substantial changes in spatial movement patterns, even if the animal continues to navigate in the same environment. To further examine this notion, we leveraged recent findings in bats in which a comprehensive change in sensory context (turning off the lights) appeared to induce significant changes in hippocampal CA1 spatial tuning[33]. We therefore examined whether greater changes in neural tuning could also be accounted for by altered behaviour between different contexts. To address this question, we conducted an additional set of longitudinal calcium-imaging experiments during which the lights alternated on for 20 min (lights on), off for 20 min (lights off) and then on again for 20 min (lights on′) during each foraging session (Methods). When comparing two-dimensional (2D) rate maps across conditions, we observed what appeared to be sensory-based remapping, in agreement with previous electrophysiological findings in bats[33] (Fig. 4a and Extended Data Fig. 9). However, a closer examination of the spatial movement patterns of the bats revealed that, although flight behaviour was highly similar within a given contextual condition (lights on or lights off), it was highly dissimilar across conditions (10 sessions per bat for $n = 2$ bats; Fig. 4b and Extended Data Fig. 10). The bats still flew along structured paths in both conditions, but many paths were flown disproportionately more often in either the lights on or the lights off condition (Fig. 4b and Extended Data Fig. 10a–g). Taking advantage of both the stability of the bats' flight behaviour and our ability to longitudinally track individual neurons over days, we were able to accumulate many examples of trajectories that occurred across both conditions (Extended Data Fig. 10h, i). When restricting our analysis to these shared flight trajectories, stable neural tuning persisted (Fig. 4c–e) and we found no statistical difference in population tuning stability when comparing within or across conditions (Fig. 4f). To further address whether differences in flight behaviour may account for perceived changes in spatial tuning, we compared 2D rate maps of simulated

Author Manuscript Author Manuscript Author Manuscript Author Manuscript

stable tuning fields for all flights across both lights on conditions, and between lights on and lights off conditions. Similar to what we observed empirically (Fig. 4f), we found that illumination-dependent changes in flight variability gave the appearance of stability within lights on conditions but instability when comparing across conditions (Fig. 4g). Taken together, these findings demonstrate that condition-dependent changes in behaviour can lead to the illusion of tuning instability, even when the underlying neural code remains highly stable.

Discussion

By imaging neural activity from flying bats, we found that hippocampal spatial tuning for the same movements in a familiar environment is highly stable. Furthermore, most of the neurons that were reliably tracked over days remained active and spatially selective when bats flew the same trajectories, suggesting a stable participation of individual neurons in representing spatial movements through a familiar environment, even after substantial changes in sensory context. These findings support earlier electrophysiological studies in rats that posited a stable hippocampal code as a substrate for the stable spatial representation of a familiar environment[11,15,18]. However, our findings differ from imaging studies in head-restrained or freely moving mice over the past decade that showed that large fractions of hippocampal neurons can change their responsiveness from one day to the next[7–9,12]. We hypothesize that these differences could arise from several sources. One possibility is that the stability of spatial representation varies between species, and mice may generally have a less stable hippocampal code. Indeed, electrophysiological studies in mice revealed drifting spatial representations even within a single foraging session[34], whereas rats exhibit more stable spatial neural activity[20]. Yet, factors such as task engagement, goal-directed behaviour and attentional demands have been shown to account for some of the observed differences[34,35]. Alternatively, it may be that the estimation of spatial tuning stability is simply affected by movement repertoires exhibited by different species. For bats, flight can result in a highly structured, homogenous behaviour. The spatiotemporal consistency of the bats' flight enabled us to repeatedly sample the same behaviour in a given location across time and cue conditions, which in turn enabled us to make straightforward, statistically rigorous comparisons between behavioural and neural variability. To this end, we have shown that relatively subtle changes in spatial movement patterns across days or contexts can lead to challenges in accurately assessing the stability of firing fields. A direct prediction arising from these findings is that a stable hippocampal code may be observed across species when neural tuning is assessed relative to a more structured navigational behaviour[36,37] that allows simultaneous control over multiple factors that are known to modulate hippocampal activity, such as position, velocity, direction of movement and time[29,30].

The neurophysiological findings presented here support a model in which the spatial representation of stable movement patterns through a familiar environment remains largely unchanged[11,15]. Although such a stable neural code might facilitate the stable navigation behaviour exhibited by Egyptian fruit bats[3,5,6,19], a direct causal role of the bat hippocampus in aerial navigation remains to be demonstrated. Combined, our findings highlight the importance of using a comparative approach that leverages the specialized behaviours of

Author Manuscript Author Manuscript Author Manuscript Author Manuscript

different species to investigate how conserved circuits, such as the hippocampus, enable neural computations that subserve navigation and spatial memory[38,39].

Online content

Any methods, additional references, Nature Research reporting summaries, source data, extended data, supplementary information, acknowledgements, peer review information; details of author contributions and competing interests; and statements of data and code availability are available at https://doi.org/10.1038/s41586-022-04560-0.

Methods

Bats, experimental design and behavioural tasks

Imaging data were collected from the hippocampal dorsal CA1 area of $n = 7$ adult (aged 2–3 years) male, laboratory born Egyptian fruit bats (*R. aegyptiacus*; weight, approximately 160 g) engaged in aerial spatial foraging[26]. Before the experiments, the bats were housed in a large, environmentally enriched colony room in which they were able to fly freely and socialize. Bats were naive to the experimental flight room before the start of flight experiment training[26]. When not in the flight room, the experimental animals were socially housed in cages (31 cm × 36 cm × 45 cm or 47 cm × 77 cm × 93 cm) in a separate communal housing room. The lights in the housing room were maintained on a 12 h–12 h reverse light cycle (lights on–lights off; 07:00–19:00). All flight experiments were performed at the same time of day during their awake hours (dark cycle). All experimental procedures were approved by the Institutional Animal Care and Use Committee of the University of California, Berkeley.

All of the experiments were performed in an acoustically, electrically and radio-frequency-shielded room (5.6 m × 5.2 m × 2.5 m) with high-precision lighting control[26]. The flight room walls and ceiling were covered with black acoustic foam to dampen the noise from outside the experimental room and reduce acoustic reverberation. An additional layer of acoustically absorbing black felt was used to protect the acoustic foam from being damaged by the bats while maintaining the intended acoustic environment[26,27]. The flight room floor was also covered with the same acoustically absorbing black felt. The 3D spatial position of the bat was tracked at the millimetre resolution using 16 motion-capture cameras (Raptor-12HS) distributed across the ceiling (Motion Analysis), as described previously[26]. Each camera tracked six to eight reflective markers that were attached to the wireless microscope cover carried by the bat and the video was sampled at a frame rate of 120 Hz. The 3D position of the marker set was computed and saved using a proprietary commercially available software specifically designed for the motion tracking hardware (Cortex-64; Motion Analysis). Marker positions were processed using custom MATLAB (MathWorks) functions as previously described[26]. Finally, the resulting tracking data were smoothed by 10 samples (83 ms). Calibration of the video tracking system was performed daily (using the calibration wand and by placing 14 reflective markers on the same reference places) before each recording session to assure reliable reconstruction accuracy of 3D position and day-to-day registration of the coordinate system.

Author Manuscript Author Manuscript Author Manuscript Author Manuscript

Foraging experiment.—The foraging experiment consisted of three sessions: prebehavioural rest (5 min), foraging (roughly 50 min) and post-behavioural rest (5 min). For all of the experiments, bats were food restricted to no less than 80% of their baseline body weight to motivate their foraging behaviour during the experiments. Neural activity was imaged continuously during all sessions and the bat remained in the flight room for the entire duration of the experiment. During the prebehavioural rest session, the bat was kept in a small cage (25 cm × 32 cm × 46 cm) within an opaque enclosure (40 cm × 46 cm × 65 cm) inside the flight room. After the prebehavioural rest session, the bat was taken out of the enclosure, released from the cage and allowed to forage freely from the feeders. This was followed by the post-behavioural rest session, which was performed in the same manner as the prebehavioural rest session.

Details of the basic behavioural experimental set-up have been described previously[26]. Four automated feeders were placed on the wall at one end of the room, with two on each side of the wall (Fig. 1d). Two of the feeders (one each on the far sides of the wall) were active during the behavioural sessions (Fig. 1d). Each feeder had an infrared beam break sensor to detect when a bat landed on the feeder and a motor driven reward system that administered a pureed fruit (approximately 0.3 ml per reward). The feeders were all independently controlled by an Arduino (Uno Rev3) and Adafruit Motorshield (1438; Adafruit) interfaced with a computer placed outside of the experimental room. Positional tracking (Motion Analysis) was used to monitor crossings of a virtual 2D boundary four meters away from the feeders. The bat was required to fly across the virtual boundary to bait the feeders. Once the bat received reward at a feeder, that feeder was deactivated to encourage the bat to cross the invisible boundary and rebait the feeders. Bats could return to any feeder after rebaiting. Our dataset was collected when bats were experienced in flying for reward in the flight room (after at least five to ten foraging sessions in this environment) and had begun to reliably and spontaneously fly repeated flights. On average, bats flew 76 ± 20 flights per session, which yielded a total of 4,731 flights; 73.4% of all flights (3,472 out of 4,731) occurred along repeated flight paths.

Lights on versus lights off foraging experiment.—Two of the seven bats also participated in the lights on, lights off, lights on′ foraging experiment. These experiments were similar to those described above but consisted of five sessions: prebehavioural rest (5 min), lights on foraging (20 min), lights off foraging (20 min), lights on foraging′ (20 min) and post-behavioural rest (5 min). Egyptian fruit bats can alternate between two sensory modalities that enable high-resolution distal sensing: echolocation when flying in the dark[40–42] and vision when navigating in light[43,44]. Calcium responses were recorded continuously and the bat remained in the flight room throughout the entire experiment without disruption from the experimenters. As described above, the bat was kept in a small cage (25 cm × 32 cm × 46 cm) within an opaque enclosure (40 cm × 46 cm × 65 cm) inside the flight room during all the pre- and post-behavioural sessions. After the prebehavioural rest session, the bat was released into the room to begin the self-directed foraging task with the room light panels turned on (4.95 ± 0.07 lux; mean ± SD; measured at the floor level in the centre of the room using ILT-1700 illuminance meter; International Light). Automated lighting was controlled using arrays of ceiling-mounted LEDs (5% Lumos; C3 Lighting)

Author Manuscript Author Manuscript Author Manuscript Author Manuscript

with a timer (Q Light Controller+) that turned off the lights (0.08 ± 0.02 lux; mean ± s.d.; residual light from the near-IR (750 nm peak) positional tracking system) for the lights off portion of the experiments and turned them back on to the same lighting levels for the second iteration of the lights on portion of the session.

Microscope design.—We used a custom miniature microscope (miniscope) made of 3D printed material (black resin; Formlabs)[25] (Fig. 1a) similar to previously described designs[45–48]. This microscope is open source and the design files, part numbers and software are publicly available at GitHub (https://github.com/gardner-lab/FinchScope and https://github.com/gardner-lab/video-capture). In brief, a blue LED produced excitation light (470 nm peak; LUXEON Rebel). A drum lens (45–549, Edmund Optics) collected the LED emission, which passed through an excitation filter (3.5 mm × 4 mm × 1 mm, ET470/40x; Chroma), deflected off a dichroic mirror (4 mm × 6 mm × 1 mm, T495lpxr, Chroma) and entered the imaging pathway via a roughly 0.25 pitch gradient refractive index (GRIN) objective lens (GT-IFRL-200, GRIN-Tech). Fluorescence from the sample returned through the objective, the dichroic, an emission filter (4 mm × 4 mm × 1 mm, ET525/50m, Chroma) and an achromatic doublet lens (45–207, Edmund Optics) that focused the image onto an analogue CMOS sensor with 640 × 480 pixels (MB001; 3rd Eye CCTV). The frame rate of the camera was 30 Hz and the field of view was approximately 700 μm along the diagonal axis. Video was broadcast at approximately 2.37 GHz through a wireless transmitter (TX24019, 100 mW). The entire system was powered with a lightweight consumer grade 3.7 V, 300 mAh lithium polymer battery, which provided stable recording for over an hour at average imaging LED intensities (less than 100 μW post-objective power). The NTSC video and a synchronization signal were both digitized through a USB frame grabber. Custom software written in the Swift programming language running on the macOS operating system (v.10.10) leveraged native AVFoundation frameworks to communicate with the USB frame grabber and capture the synchronized analogue video stream. The video and sync signals were written to disk in MPEG-4 container files. The video was encoded at full resolution using either the H.264 or lossless MJPEG Open DML codec and the sync signal was encoded using the AAC codec with a 48 kHz sampling rate.

Surgical procedure

General surgical and anaesthesia procedures were similar to those previously described for Egyptian fruit bats[16,27] and the GRIN lens implant procedure was adopted from work in rodents[45,48]. Analgesics were given for three days after surgery and antibiotics were given for one week after surgery.

Anaesthesia for all of the procedures was induced using a subcutaneous injection cocktail of ketamine, dexmedetomidine and midazolam. The bat was then placed in a stereotax (942, Kopf) where the level of anaesthesia was monitored by toe pinch reflex and breathing rate. A rectal probe measured the bat's body temperature continuously and a heating pad was used to maintain the bat's body temperature stable at around 34.5 °C. Anaesthesia was maintained throughout surgery by successive injections (around once per hour) of an anaesthesia maintenance cocktail consisting of dexmedetomidine, midazolam and fentanyl. Lactated Ringer's solution was subcutaneously administered to maintain hydration.

Author Manuscript Author Manuscript Author Manuscript Author Manuscript

While the bat was under anaesthesia, the skull was exposed and cleaned, and the surrounding skin and tissue was retracted. The coordinates above dorsal CA1 (dCA1) were measured on the outside of the skull from a common reference point at the confluence of sinus. A circular craniotomy (1.2 mm diameter) was made through the skull over the left hemisphere. The centre of the craniotomy was positioned 5.8 mm anterior to the transverse sinus that runs between the posterior part of the cortex and the cerebellum, and 2.8 mm lateral to the midline. The brain surface was exposed but the dura was left intact. A NanoFil syringe (36 GA beveled needle, WPI) was attached to the stereotax and slowly lowered into the dorsal CA1. After waiting for 3 min, 1.2 μl of pAAV9.hSyn.GCaMP6f.WPRE.SV40 was injected (titre 1.40×10^{13}, 100837, V20744, Addgene) at a rate of 4 nl s^{-1} using a microinjection pump (UMP3; WPI). Genetic expression driven by the hSYN promoter has been shown to express in both excitatory and inhibitory neural cell types in the mammalian hippocampus[49]. Then 5–10 min after completing the injection, the needle was slowly retracted out of the brain. The craniotomy was then filled with a biocompatible elastomer (Kwik-Sil; WPI) and the tissue was closed with sutures.

One week after the injection, the bat was placed under anaesthesia using the same procedures for the lens implantation procedure. The skin was retracted in the same manner as the injection surgery to re-expose the craniotomy and the biocompatible elastomer was removed from craniotomy. A GRIN lens (1 mm diameter × 9 mm height, 0.5 pitch; 1050–002177, Inscopix) was placed inside the same craniotomy directly dorsal to CA1. The surface of the skull was carefully cleaned and scored to facilitate cement bonding to the skull. Three bone screws (19010–00; FST) were inserted into the skull to provide anchor points for the cement. A thin layer of bone cement (C&B Metabond, Parkell) was applied onto the surface of the skull and around the base of the bone screws. Kwik-Sil was then removed from the craniotomy to expose the brain surface. The cortex above dorsal CA1 was aspirated using a vacuum pump attached to a 30 GA blunt needle. Ice-cold sterile lactated ringer solution along with pressure from an absorbable sponge (Gelfoam, Pfizer) was applied to the brain to prevent bleeding during the aspiration. Aspiration continued slowly until the parallel fibres of the hippocampal oriens were visually identified. The relay GRIN lens was held by a custom-built 3D printed lens holder attached to a vacuum pump. The lens was slowly lowered and positioned dorsal to the CA1 region of the hippocampus (approximately 2.5 mm below the surface of the brain). After implanting the lens, Kwik-Sil was applied to the base of the craniotomy to protect the brain at the interface of the lens and the skull. Carbon powder was mixed with dental acrylic to create an opaque black acrylic that was applied around the surface of the skull and above the bone screws to hold the implanted lens in place. The top of the GRIN lens was covered with Kwik-Sil elastomer and a small plastic cap to protect it from mechanical damage while the bat recovered.

Next, 2 to 3 weeks after lens implantation, the miniaturized microscope was aligned with the GRIN lens. While under anaesthesia, the Kwik-Sil elastomer protection was removed from the relay lens and the surface of the lens was cleaned with 70% ethanol. A cable from the imaging DAQ was attached above the CMOS to control the LED power and stream video data, which were acquired using custom video capture software (https://github.com/gardner-lab/video-capture)[25]. The miniscope was attached to a stereotax arm using a custom CNC-machined clamp and moved above the implanted relay lens to find the best field

Author Manuscript Author Manuscript Author Manuscript Author Manuscript

of view with the maximal number of fluorescent cells visible. To account for the settling of the dental acrylic after drying, the miniscope was raised approximately 50 μm above the ideal focal plane before anchoring it above the relay lens with the dental acrylic. A custom 3D-printed protective housing case was optically glued (Flow-It ALC, Pentron) onto the 3D printed protective base cone. Then, 1–3 days after attachment, the miniscope was focused to an optimal field of view (by rotating the CMOS along the threaded exterior of the microscope body) and secured to the protective case with a thick layer of optical glue to prevent any further movement for the rest of the experiment.

Histology.—At the end of the experiment, the bats were administered an overdose of pentobarbital and perfused transcardially using a flush of 250 ml of phosphate-buffered saline (PBS, pH 7.4) spiked with 0.5 ml heparin (1,000 USP U ml^{-1}) followed by 250 ml of fixative (3.7% formaldehyde in PBS). The brain was carefully removed and post-fixed overnight in the same fixative. To avoid overfixation, the brain was moved after 24 h from the fixative into a 30% sucrose solution for cryoprotection. After approximately 2 days, or once the brain had sunk to the bottom of the solution, 40-μm coronal sections were made using a microtome (HM450, Thermo Fisher Scientific) with a freezing stage. The sections were floated in PBS, stained for DAPI (1:10,000, Thermo Fisher Scientific) and cover-slipped with aqueous mounting medium (ProLong Gold Antifade Mountant, Thermo Fisher Scientifc). Fluorescent images of each section surrounding the implant were taken using an Axioscan Slide Scanner (Zeiss). Subsequently, these images were used to identify GCaMP6f-labelled cells and verify the lens implant location above dCA1.

Data analysis

All analyses were conducted using custom code in MATLAB (Math-Works), which is available online (https://github.com/WALIII/ImBat).

Flight segregation and behavioural analysis.—Position coordinate vectors (*x*, *y* and *z* of the centre of mass of the markers on the head) for each bat were concatenated across sessions and flight was identified by a velocity threshold of 0.2 m s^{-1}. As in other bat species, many flights followed along the same paths[50]. Similar flight paths were typically traversed in only one direction. Flights were clustered into paths by agglomerative hierarchical clustering, where flight trajectories were downsampled to six points per flight (first and last points corresponded to the take-off and landing positions, respectively). Intermediate points were calculated through spline interpolation. Eighteen-dimensional (6 by 3D) vectors representing different flights were clustered into paths according to their Euclidean distance using the linkage and cluster functions in MATLAB. The linkage distance was set to 1.2 m after manual inspection of flight groupings and we enforced a minimum of three flights per cluster across all sessions.

All of the remaining flights that did not belong to a path cluster were considered to be unique, which accounted for 26.6% (1,259 out of 4,731) of all flights. Flight tuning stability was determined by taking all flights from the same path and comparing the mean 1D correlation of the *x*, *y* and *z* positions, aligned to takeoff, to their respective mean path on the first session.

Author Manuscript Author Manuscript Author Manuscript Author Manuscript

Artifact rejection, motion correction.—Raw video frames from the wireless microscope were acquired at 30 fps and then spatially downsampled by a factor of two. Wireless transmission artifacts impacted individual frames and were detected by taking the s.d. of the detrended time series vector of the median intensity of all pixels on the boundary (first and last rows and columns) of each frame. Values that exceeded 2 s.d. were treated as dropped frames, which comprised less than 0.01% of all frames. Data were then motion-corrected using subpixel image registration[51] and temporally median filtered by four frames. Periodic clock pulses generated by a Master-9 device (A.M.P.I.) were used to create a timing signature that served as a common frame of reference for the flight tracking system and the microscope recording software to align and synchronize the motion-tracking and imaging systems offline[25,27].

ROI segmentation and multi-day alignment.—ROI identification, segmentation and alignment across days was performed similarly to previously published approaches[7,9,47,52–54] and are therefore described in brief below. To detect ROIs corresponding to putative neurons, we used an adaptation of a constrained non-negative matrix factorization approach designed for single-photon calcium imaging data (CNMF-E)[53,54]. This approach identifies, detrends and removes an estimate of the local fluctuating background from each ROI. The following parameters were used for all bats on all days: mean-subtracted 2D gaussian smoothing kernel (gSig) = 8 μm, maximum soma diameter (gSiz) = 34 μm, minimum pixel-to-noise ratio for seeding a neuron (PNR) = 2.5, minimum local correlation = 0.85. A ring model was used to estimate a background signal for each neuron (ring_radius = 46 μm). Calcium traces were deconvolved using an autoregressive model (OASIS) with order $p = 2$ and using the ‘constrained’ method, which gives a frame-resolution (33 ms at 30 fps) timing estimation of the underlying spiking-related burst event[52,55]. Finally, identified ROIs were manually inspected to remove duplicates and inappropriate merges.

ROI alignment across days was performed using a combination of statistically driven and supervised approaches. Tracking confidence can be influenced by a number of factors such as damage or replacement of the microscope, experimenter refocusing or slow drift of the field of view (FOV) associated with day-to-day brain movement. Given the possibility that methodologically driven tracking instability can be conflated with biologically driven tuning instability, we considered only adjacent sessions where manual inspection indicated that the imaging plane was highly stable. This involved evaluating the consistency of anatomical features such as blood vessels, as well as static persistent features with high fluorescence background such as neuropil. After this assessment is satisfied, we then evaluate the sharpness and consistency of the constellation of cells in a maximum $\Delta f/f_0$ projection image for blurriness or lateral displacement, which also serves to indicate a change in imaging focal plane.

Once stable adjacent FOVs were manually verified, CNMF-E-identified ROI spatial footprints were aligned across days using a previously published algorithm (CellReg)[54]. After rigid registration of ROI masks across days, this approach uses a combination of spatial correlation of ROI spatial footprints and the distance between ROI centroids to build a distribution of potentially same or different cell pairs within a radius of 10 μm. These

Author Manuscript Author Manuscript Author Manuscript Author Manuscript

cell pairs do not need to be on adjacent days. We further restricted our analysis to CNMF-E-identified ROIs that could be unambiguously identified in at least two independent, but not necessarily consecutive, sessions to further guarantee that cells that we could not confidently track were not attributed to biological tuning instability. This restriction criteria almost exclusively removed ambiguous ROIs that either had a very low signal to noise ratio (SNR) or were at the very edges of the field of view. Nevertheless, cells that fired extremely rarely (that is, in only a few sessions out of the whole experiment) were still included and assessed in our analysis.

Furthermore, we performed a manual annotation of ROIs from the full session maximum $\Delta f/f_0$ projections. This serves as an alternative approach to evaluating neural activity per session in a way that is independent of the deconvolution ability of CNMF-E or CellReg's registration accuracy across days. Given that our viral expression is sparse, our data contain numerous examples of well-isolated, high-SNR neurons within a region of 50–100 μm^2. We can leverage this sparsity to independently estimate the proportion of cells that are unambiguously transient from one day to the next (that is, where ROI tracking was abruptly lost or gained over an adjacent session, due to a complete loss or gain of both flight tuning and spontaneous activity). This analysis is predicated on the fact that cells that are most easily and unambiguously identified on any day should occur equally likely to drop in/out compared to low SNR cells (which are more susceptible to methodological issues). Considering a subset of 36 flight sessions with the clearest maximum $\Delta f/f_0$ intensity projections, we were able to identify only a few rare examples of drop-in/out in high SNR ROIs over a single day relative to nearby ROIs (Extended Data Fig. 7). Specifically, out of 1,038 hand-labelled, clearly identified ROIs, we found that the majority (97.4%, 1,011 out of 1,038) corresponded to a set of unique pairs that were clearly visible on adjacent sessions. Of the remaining 2.6%, we found that 1.15% (12 out of 1,038) visibly drop-in and 0.87% (9 out of 1,038) visibly drop-out from one session to the next, and an additional 0.57% (6 out of 1,038) are transient (that is, they are not active on the proceeding or following session). This finding is consistent with previous studies in mice which find that most cells in the hippocampus are active on most days and neural tracking is predominantly limited by imaging plane instability rather than by previously active cells falling completely silent[9]. Similarly, the majority of our tracking loss across days occurs when the sharpness and intensity of a well-isolated ROI slowly fades over time, which is best explained by residual day-to-day plane instability. We estimated the discrete tracking loss (from the initial identification to the point at which an ROI can no longer be detected or confidently matched on an adjacent session) to be about 2% of CNMF-E identified ROIs per day under ideal conditions where there is no noticeable change in the stability in the imaging plane (Extended Data Fig. 6a). Our final imaging dataset consisted of 63 daily sessions from seven bats (9 ± 3 sessions per bat), with 562 unique ROIs (that is, ROIs that we believe to be independent and confidently tracked for at least one session). The numbers of unique ROIs imaged from each of the seven bats were 101, 187, 20, 70, 39, 101 and 44 (tracking statistics of ROIs used in this dataset are provided in Extended Data Fig. 6a, b). In the two bats tested in the alternating lights on versus lights off foraging experiment, a total of 131 unique ROIs (59 and 72 ROIs from bat 1 and bat 2, respectively) were imaged across 2,313 total flights

Author Manuscript Author Manuscript Author Manuscript Author Manuscript

(mean of approximately 152 and 79 flights per day, respectively) for 10 consecutive days each.

ROI significance and stability.—The significance of flight path tuning for each ROI was determined by comparing the 1D spatial information (inferred spikes per second) of the mean path-aligned deconvolved neural activity for any paths with at least 10 flights. Flight-aligned neural activity was concatenated across sessions in which ROIs were reliably detected and aligned. To calculate spatial information, we used the following equation derived from mutual information[16,56]

$$\mathrm{SI} = \sum_i p_i(r_i/r)\log_2(r_i/r),$$

where p_i is the probability of the animal to be in the ith time-bin (relative to flight takeoff) and r_i is the deconvolved firing rate of the neuron in the ith voxel. Here, r is the average firing rate, computed as:

$$r = \sum_i p_i r_i$$

Significance was determined by comparing the observed SI value to a shuffled distribution (1,000 shuffles per ROI), which was computed by circularly shifting the burst event time by a random amount for each path-aligned flight. To calculate significance during flight, we circularly shuffled only the periods of flight. Bonferroni correction was used for each neuron based on the total number of flight paths considered to correct for multiple comparisons. An ROI was considered to be flight-tuned if its activity contained significantly more information than chance ($P < 0.05$ after correcting for multiple comparisons) during flight for any of the three most common flight paths. For all significantly tuned ROIs, tuning stability across days was determined by taking the Pearson correlation of the mean flight-aligned ROI $\Delta f/f_0$ time series either across days (Fig. 2b) or across lights on and lights off conditions.

To calculate neural variability (Extended Data Fig. 8a, b), we first obtained the peak of the mean, flight-path-aligned, deconvolved time series for all of the significantly flight-tuned ROIs. To account for multiple firing fields per flight path, in this analysis, we also considered peaks during flight that were separated by at least 1 s and had a prominence that exceeded 1.5 s.d. (s.d. of the mean time series over the entire session). We then took the distribution of intensity values at these peak times across all flight-aligned, smoothed (by three frames, that is, approximately 100 ms), deconvolved neural activity traces for the three most common flight paths, provided that they contained at least ten flights on any given session. Finally, we calculated the coefficient of variation of this distribution. To calculate flight position variability, we took the x, y and z positional coordinates at the peak times identified in the neural time series, and then computed the Euclidian distance to the mean x, y and z coordinate for the corresponding flight path. We next compared neural activity variability (normalized coefficient of variation of neural activity over flights) to flight variability (that is, the mean Euclidian distance of the points in space when a neuron was active, relative to the mean flight path) for every firing field and flight path pair.

Author Manuscript Author Manuscript Author Manuscript Author Manuscript

Some flight paths are composed of behaviour that is more variable from flight to flight. We reasoned that tuning fields would appear to be less stable for flight paths with greater behavioural variability because of a decrease in spatial specificity and repeatability from flight to flight, which will compromise our ability to measure the tuning fields. For ROIs that were significantly tuned to more than one flight path, we compared the difference in the distributions of ROI stability for the firing field for more versus less variable flights, using the same process and logic described above.

Analysis of positional tuning at overlapping flight segments and goal-vector tuning.—To further assess positional tuning of hippocampal neurons, we compared ROI tuning for pairs of flight paths with similar velocity profiles and durations that were either overlapping or non-overlapping in space (Extended Data Fig. 4a–g). 1D tuning profiles for each ROI were constructed by taking the mean of the deconvolved activity trace for each ROI aligned to takeoff for each flight path. Correlation scores were then calculated by taking the Pearson correlation of these ROI tuning profiles across either spatially similar flight paths (that are partially spatially overlapping) or spatially dissimilar flight paths (that are non-spatially overlapping). We then also calculated within-flight-path tuning similarity by comparing the ROI tuning profiles between even/odd trials of a given flight path. Furthermore, we recalculated all correlation scores after restricting comparisons to the spatially overlapping portions of the two most similar flights (portions in which the within-flight-path positional variability is equal to or greater than the across flight path variability).

To assess vectorial goal tuning of hippocampal neurons[28], we analysed angle and distance tuning along different flight trajectories (Extended Data Fig. 5). 1D tuning profiles for each ROI were made by binning the deconvolved activity trace relative to either the distance to the goal location (using 50 cm bins) or by the angle between an animals' heading and the goal (using 18° bins) for each flight path and normalizing relative to their occurrence in behaviour. These 1D distance and angle tuning profiles were then compared across flight paths by taking their pairwise Pearson correlation. Comparisons were made between (1) flight path pairs that terminated in the same goal location but did not overlap in space, as well as between (2) flight path pairs with highly similar trajectories where one path did not terminate in the same goal location. Suitable flight behaviour for this analysis could be found in a subset of our dataset (334 ROI across 12 flight paths, $n = 4$ bats). To create a null distribution for comparison, we recomputed the pairwise correlation scores after shuffling ROI identity.

The bat's position co-varies with angle and distance relative to the goal location during flight behaviour, which can lead to egocentric tuning misattribution (for example, goal-vector tuning). We therefore considered what percentage of ROIs have similar, statistically significant distance tuning across different, non-spatially overlapping flight paths that end in the same goal location. First, a shuffled distribution was created for each ROI by rigidly time-shifting deconvolved neural activity during flight in a circular manner and recalculating goal-distance tuning. This procedure was repeated 10,000 times to create a null distribution for each ROI. We first identified a subset of ROIs where the peak of their distance tuning curves exceeded the 95th percentile compared to shuffle for both non-overlapping flight

Author Manuscript Author Manuscript Author Manuscript Author Manuscript

paths. ROIs were then deemed to be ‘significantly tuned’ if their tuning was also similar across flight paths (that is, no statistical difference in tuning profiles on the basis of a Wilcoxon rank-sum test; $P > 0.05$). Taking this approach, we found that 4.1% (14 out of 335) of ROIs were significantly tuned to distance across different trajectories. Furthermore, we performed the same analysis for angle tuning and found that 3.9% of the ROIs (13 out of 335) had the same tuning across different trajectories. Finally, we assessed the stability across days of this small subset of significantly tuned angle or distance to goal neurons and found no differences with the stability of the larger population ($P > 0.5$, Wilcoxon rank-sum test).

Decoding analysis.—We devised a constrained naive Bayesian decoder[57] to predict the flight path membership from neural activity, using the fitcnb function in MATLAB (Extended Data Fig. 4h, i). A classifier was trained for each bat by taking the peak height and time of the deconvolved neural activity for all ROIs relative to takeoff. We considered only data from flight paths that contained at least ten flights on any given session to avoid biases due to low samples (approximately five to six flight clusters per bat, for a total of $n = 40$ flight path clusters across all animals ($n = 7$)). We then predicted the flight path membership for all flight trajectories, relative to their actual groupings (that is, ground truth). Decoding accuracy was determined using tenfold cross validation by withholding flights randomly both within and across sessions.

2D rate map calculations and firing fields simulations.—2D (x,y) rate map projections were computed by binning the deconvolved firing rates for each ROI during flight periods in 10×10 cm^2 bins and collapsing across the z dimension. We also calculated a 2D occupancy map of the time spent in each of these bins. Bins with an occupancy of three or less frames of imaging data (that is, <120 ms) were removed from both the rate and occupancy maps. Both rate and occupancy maps were then smoothed by Gaussian kernel with a radius of 1.5 bins. Next, each firing rate map was divided by its corresponding occupancy map to create a normalized 2D rate map[33]. Finally, we calculated the 2D correlation of these rate maps across days and conditions.

Firing fields were simulated in a flight-room-sized space, with tuning characteristics that were empirically derived from both our calcium-imaging dataset and previously published literature of hippocampal tuning in bats[16]. Specifically, we used a field diameter between 700–1,300 cm^3 and a low spontaneous event probability that increases exponentially within the field. Fields were uniformly distributed in 3D space[16,27] and 50% were randomly given an azimuthal direction tuning between 90–180°. These simulated firing fields are always present but will only be revealed if a field’s predetermined tuning criteria (place + heading) is met. This gives us an estimate of the detection limitations of traditional rate map analysis (binning spikes in 2D and normalizing by occupancy) given certain statistics of behaviour. The behavioural data on each day were used to generate a surrogate dataset of 10,000 estimated tuning fields (obtained by convolving the bat’s trajectories with the latent fields) and we then compared these simulated fields across days in the same manner as described above. 2D rate maps were constructed as described above, enabling us to calculate the 2D correlation of these simulated rate maps across days and conditions. For our simulated

Author Manuscript Author Manuscript Author Manuscript Author Manuscript

dataset, to exclude unobservable fields that would not be revealed by flight behaviour (for example, in an untraveled corner of the environment), comparisons were made only for simulated fields that had a total of 2.5× more simulated spikes than chance on at least one day. Our simulations were repeated 10,000 times to generate a distribution for comparison.

Statistical analysis

No formal methods were used to predetermine sample sizes; chosen sample sizes were similar to those used in the field. No randomization of experimental sessions was performed and no blinding to experimental conditions was implemented during the analysis. All statistical comparisons were performed using nonparametric tests (Wilcoxon rank sum-test, Wilcoxon signed-rank test, bootstrap or randomization tests). Named tests were two-tailed unless otherwise stated. Where appropriate, adjustments for multiple comparisons were performed using the Holm–Bonferroni step-down procedure.

Reporting summary

Further information on research design is available in the Nature Research Reporting Summary linked to this paper.

Data availability

The dataset from this study is available from the corresponding author on reasonable request. Source data are provided with this paper.

Code availability

All analyses were conducted using custom code in MATLAB (MathWorks), which can be found at GitHub (https://github.com/WALIII/ImBat ; https://github.com/gardner-lab/FinchScope).

Author Manuscript Author Manuscript Author Manuscript Author Manuscript

Extended Data

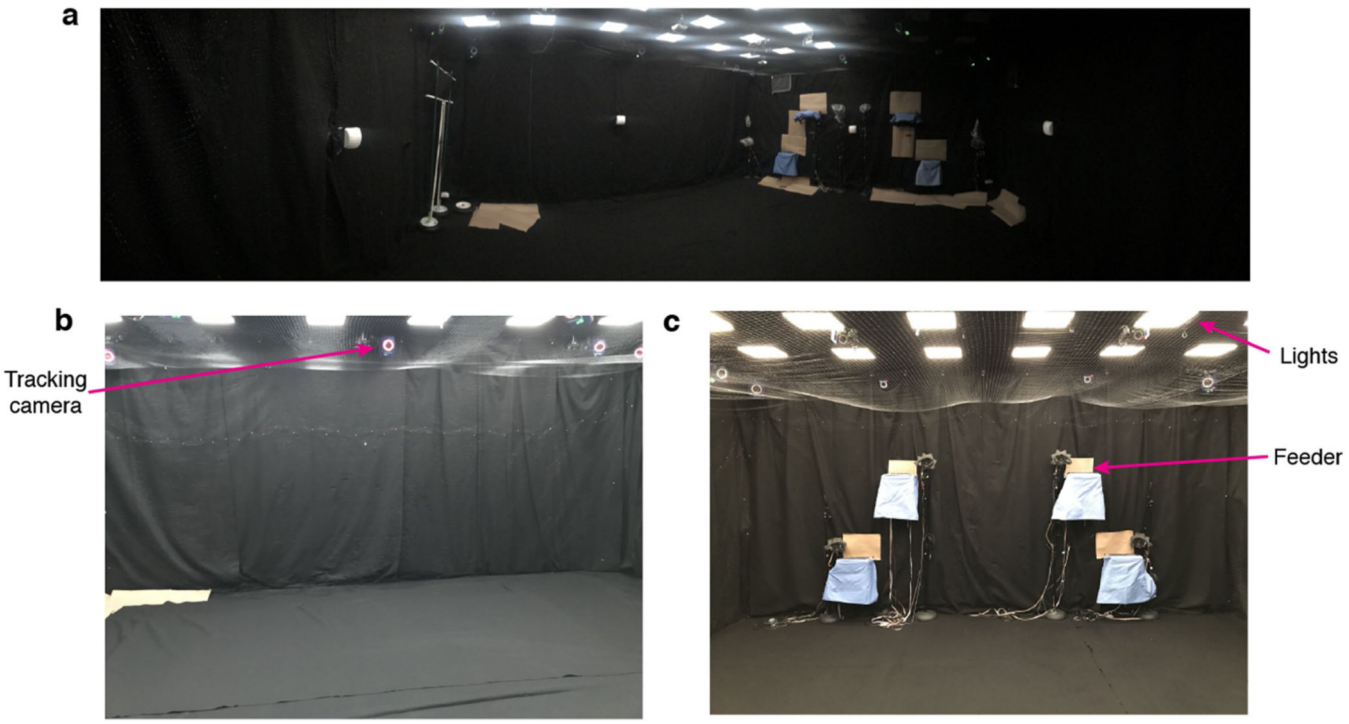

Extended Data Fig. 1 |. The automated, human-free, flight room.
a, Panoramic perspective of the automated flight room showing the feeders, adjustable ceiling lights, foam walls and motion tracking cameras. **b**, View towards one of the interior walls of the flight room. Motion tracking camera is indicated. **c**, View of the feeders. Note that the ceiling lights (white squares) and tracking system are visible on the ceiling for all images. The ceiling lights were set to specific illumination levels during the flight experiments (Methods) and are shown here at maximum brightness level for visualization purposes.

Author Manuscript Author Manuscript Author Manuscript Author Manuscript

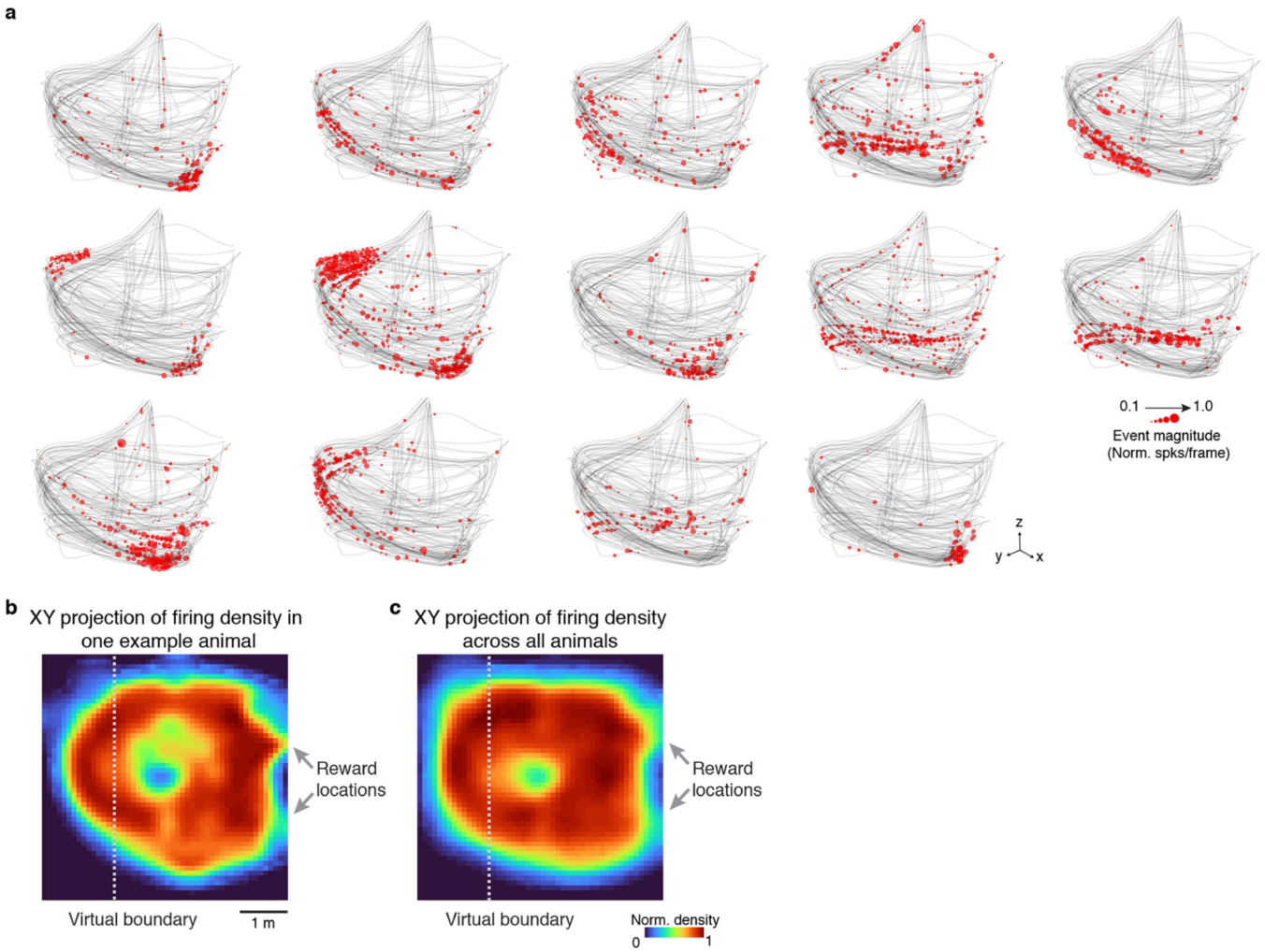

Extended Data Fig. 2 |. Imaged hippocampal neurons are spatially selective and collectively span the available environment.

a, 14 simultaneously recorded ROIs during a single free-foraging session from one bat. Red dots represent estimated spiking events superimposed on the flight trajectories (grey; Methods). The size of each dot indicates the relative size of the deconvolved spiking event per imaging frame (per 33 ms bin; Methods). **b**, **c**, Firing density is not increased around the virtual boundary and the spatial activity recorded across neurons spans the available environment. **b**, Example spatial firing density for one animal. The virtual boundary that bats had to cross in order to rebait reward feeders is indicted by a dashed line. **c**, Spatial firing density of deconvolved neural activity (that is, 'spikes') for all animals ($n = 7$). Reward locations are indicated. Images in **b**, **c** are displayed from a top-down (XY) perspective. There was no significant difference in firing density within 1m of this boundary versus other locations in the room ($P > 0.5$ for all bats, two-tailed Wilcoxon Rank Sum).

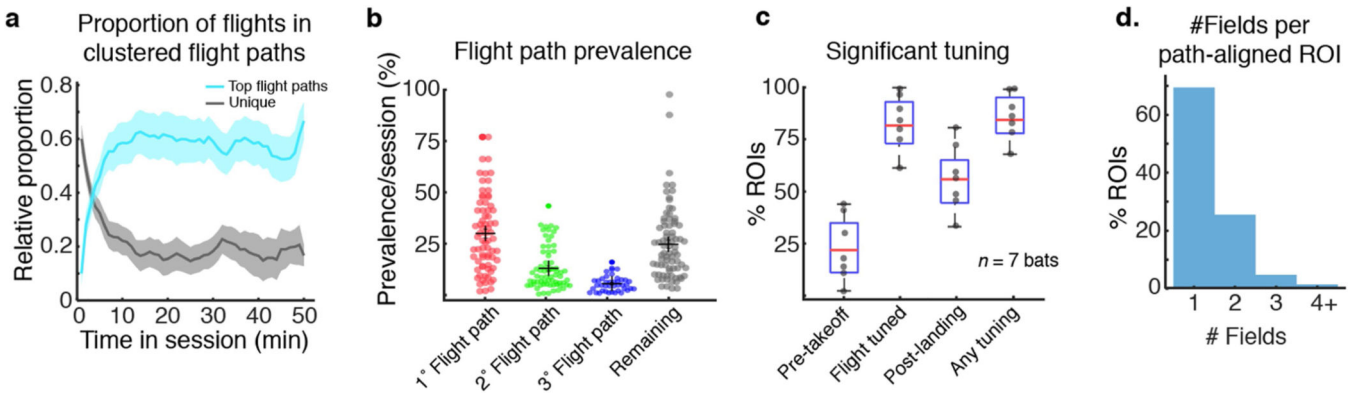

Extended Data Fig. 3 |. Spatial behaviour and hippocampal neural tuning along structured flight paths.

a, **b**, Flights predominantly occur along a few highly repeated paths. **a**, After an initial period of exploration, a few common flight paths dominate the distribution of trajectories during the free-foraging session (n = 63 sessions from 7 bats). Blue and black lines are the mean proportion of flights over time for the three most common flight paths and the unique flight paths, respectively. Shading is 95% confidence interval around the mean. 73% of all recorded flights (3,472/4,731 flights from 7 bats) occur along repeated flight paths, 54% are flown across the three most common routes (1,877/3,472 flights from 7 bats) and 70% are in the top five most common routes (2,429/3,472 flights from 7 bats). **b**, Percentage of the top three flight paths and all other flights in each session across all animals, with the mean and SEM indicated. Each point is the prevalence of the top three flight paths on each session in which they occur. Points are horizontally jittered to ease visualization. **c**, Percentage of significantly tuned ROIs for all bats (n = 7; Methods). Each dot represents a single animal, the red line represents the mean for all seven bats, boxes are first and third quartiles and bars represent maximum and minimum across all bats. **d**, Percentage of ROIs with one or more fields per flight path (Methods).

Author Manuscript Author Manuscript Author Manuscript Author Manuscript

Author Manuscript Author Manuscript Author Manuscript Author Manuscript

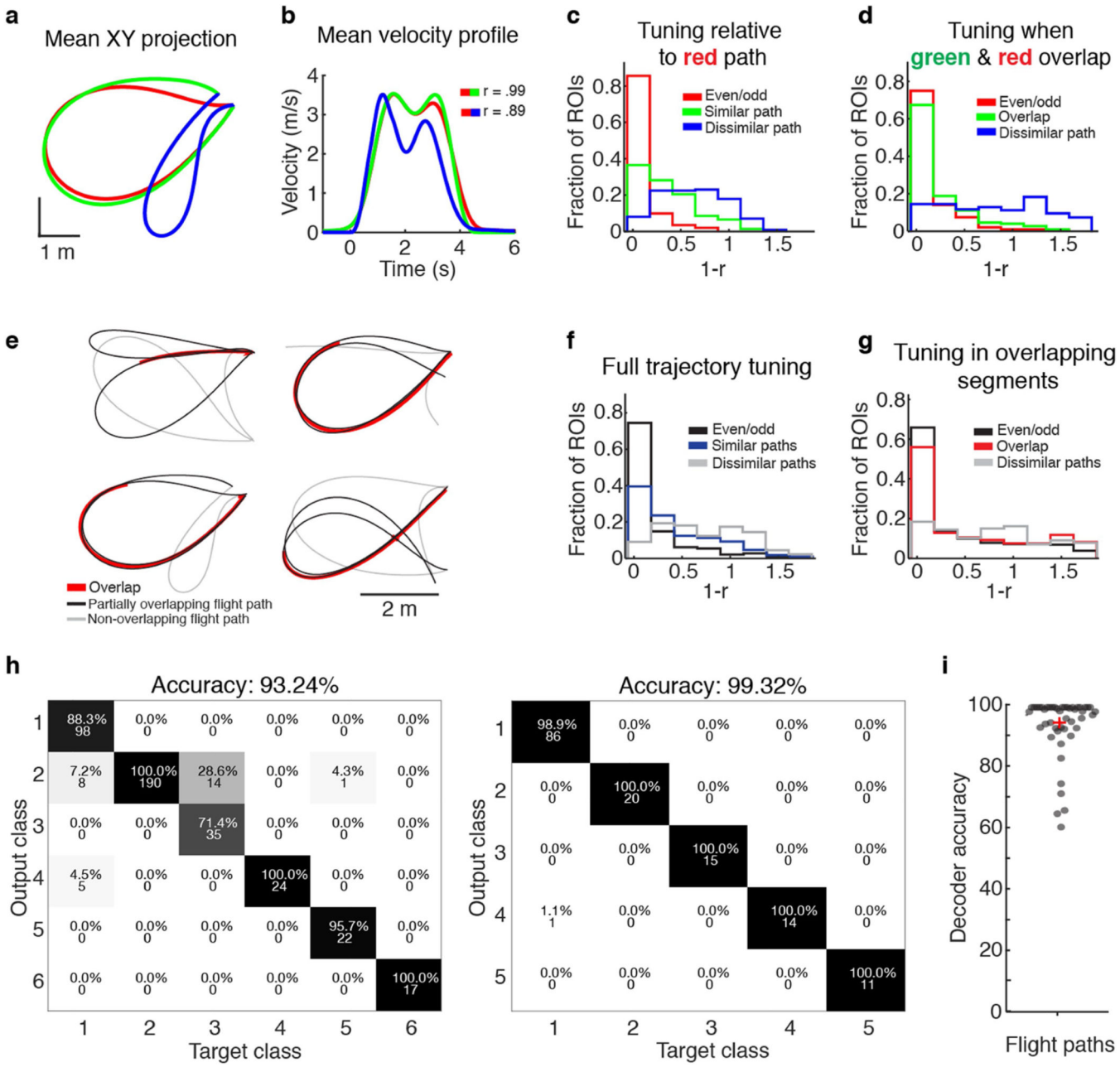

Extended Data Fig. 4 |. Neural tuning is distinct for different trajectories but is highly similar in overlapping portions.

a, 2D projection (top-down view) of the mean flight path for the three most common flight paths for one bat. Note that the green and red trajectories are highly overlapping compared to the blue trajectory. **b**, Mean velocity profile for the same top three flight paths, with colours corresponding to those in **a**. **c**, Distribution of correlation scores (shown here as 1-r for ease of comparison to Fig. 4) for all ROIs, relative to the red flight path. The red distribution is calculated by comparing even/odd flights of the red flight path shown in **a**. **d**, Same as **c** but only for the timeframe in which red and green flights overlap in space. **e**, Additional examples of overlapping flight paths. Overlapping paths are coloured

Author Manuscript Author Manuscript Author Manuscript Author Manuscript

black and non-overlapping paths are grey. Overlapping regions are coloured red. **f**, The black distribution is calculated by comparing neural tuning relative to even/odd flights that comprise a flight path; the blue distribution is the comparison of neural tuning across distinct flight paths that partially overlap in some segments. The grey distribution compares neural tuning across flight paths that are similar in duration but do not overlap in space. **g**, Same as **f** but only comparing neural activity for the timeframe in which similar flight paths overlap in space. The red distribution is the comparison of neural tuning during the overlapping portions of distinct flight paths and the grey distribution is a time matched control for trajectories that do not overlap in space. For **f**, **g**, the black distribution is calculated by comparing neural tuning relative to even/odd flights that comprise a flight path; and red indicates a comparison of overlapping portions of distinct flight paths. **h**, **i**, Different flight paths can be accurately decoded using neural activity. **h**, Prediction accuracy for two bats (left and right confusion matrixes, respectively) where each class is a flight cluster. The percent accuracy and the number of classified flights is listed within each block (Methods). **i**, Decoder prediction accuracy for all bats and all flight paths with $n > 10$ flights. Points are horizontally jittered for ease of visualization.

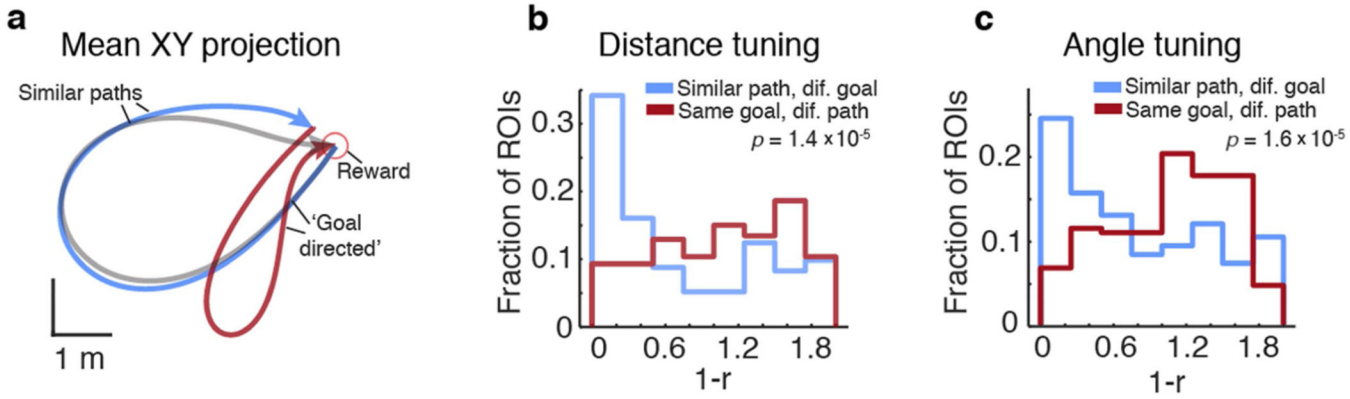

Extended Data Fig. 5 |. Neural tuning is better explained by spatial rather than goal-vector tuning.

a, Example of the analysis approach. Shown is a 2D projection (top-down view) of the mean flight path for three flights of one bat. In this example, ROI distance and angle tuning for the grey flight path can be directly compared to a dissimilar flight path that terminates at the same goal location (in red, where shared angle/distance tuning is expected in the case of goal-vector tuning[28]) and to a similar flight path that ends in a different goal location (in blue, where goal-vector tuning is not expected, but shared angle/distance tuning might artefactually result from an overlap in spatial position). **b**, Distribution of correlation scores (shown here as 1-r for ease of comparison to Fig. 4) for all ROIs binned by distance to goal (Methods) between pairs of similar flights (in blue) or pairs of dissimilar, goal terminating flight paths (in red). **c**. Same as **b** but binned by angle to the goal location. For **b**, **c**, neural tuning is significantly more similar across pairs of overlapping flight paths (distance: $P = 1.4 \times 10^{-5}$ two-tailed Wilcoxon Rank Sum; angle: $P = 1.6 \times 10^{-5}$ two-tailed Wilcoxon rank sum); for dissimilar paths towards the same goal location, both goal and distance tuning distributions are not significantly different from what would be expected by chance (performing the same comparison after shuffling ROI identity, $P > 0.05$ two-tailed

Author Manuscript Author Manuscript Author Manuscript Author Manuscript

Wilcoxon rank sum). The percent of ROIs that have the same significant tuning across two non-spatially overlapping flights to the same goal location is 4.1% (14/335 ROIs) for distance and 3.9% (13/335 ROIs) for angle (Methods). Therefore, we did not observe a pronounced goal-vector tuning independent of spatial position. This differs from a previous report in CA1 of flying bats[28] and could be due to increased false positive rates related to uncontrolled behavioural covariates, in agreement with a recent report[58].

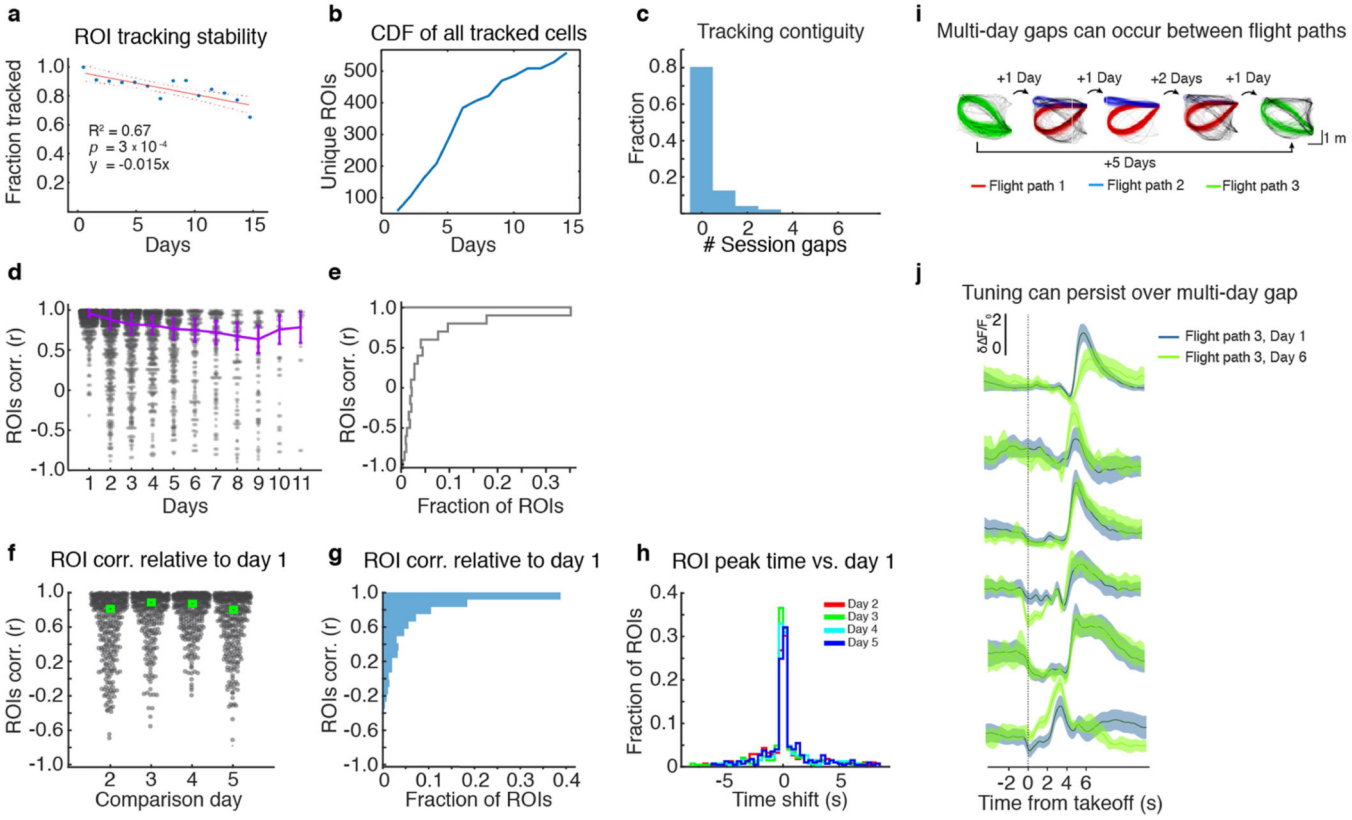

Extended Data Fig. 6 |. Tuning stability for neurons tracked over days.

a, The fraction of ROIs that can be confidently tracked, under ideal conditions (no experimenter refocusing or noticeably large change in field of view) as a function of days. Each dot represents the fraction of ROIs tracked for all bats. Tracking loss occurred at a rate of about 2% of ROIs per day (linear fit, $R^2 = 0.67$, $P = 3 \times 10^{-4}$). Dotted lines indicate 95% coefficient confidence intervals of the linear regression line in red. **b**, The cumulative distribution function (CDF) of unique ROIs that were included in the analysis, considering that some bats were tracked over longer intervals than others. **c**, Tracking contiguity showing the number of session gaps that exist between confidently tracked and aligned unique ROIs across days. **d**. Replotting the data in main text Fig. 2b, showing all underlying data points as a scatterplot. Error bars are 99% confidence intervals of the mean. Points are horizontally jittered for ease of visualization. Note that the number of ROI/flight-pair comparisons over days is decreasing ($n = 914, 635, 490, 367, 208, 167, 117, 92, 45, 11$). **e**, Histogram of correlation values for all points in panel 'd' ($n = 3{,}046$ possible ROI/flight path pairs). Note the lack of a pronounced second peak where tuning stability equals 0, as would be expected if a prominent subset of neurons were to lose or gain tuning. **f**, Scatterplot distribution of

Author Manuscript Author Manuscript Author Manuscript Author Manuscript

ROI correlations compared to day ‘1’ for the subset of consecutively tracked, flight path aligned ROIs (n = 360 ROIs). Green box indicates the distribution median. **g**, Histogram of correlation values for all points in panel **f**. Note the lack of a pronounced second peak where tuning stability equals 0, as would be expected if a prominent subset of neurons were to lose or gain tuning. Points are horizontally jittered for ease of visualization. **h**, Distributions of the mean ROI peak times relative to the first day for all points in panel **f**, separated by day (colours). **i**, **j**, CA1 tuning persists despite a multi-day gap in flight path behaviour. **i**, The dominant three flight paths are coloured in red, green and blue. Note the five-day interval between sessions with green flight paths. **j**, Six example ROI timeseries aligned to the green flight path on day 1 (dark green) and day 6 (light green). Shading is the standard deviation of the mean fluorescent time series. Note the high similarity in the ROIs’ timeseries that persists after a multi-day gap during which this flight path was not flown.

Author Manuscript Author Manuscript Author Manuscript Author Manuscript

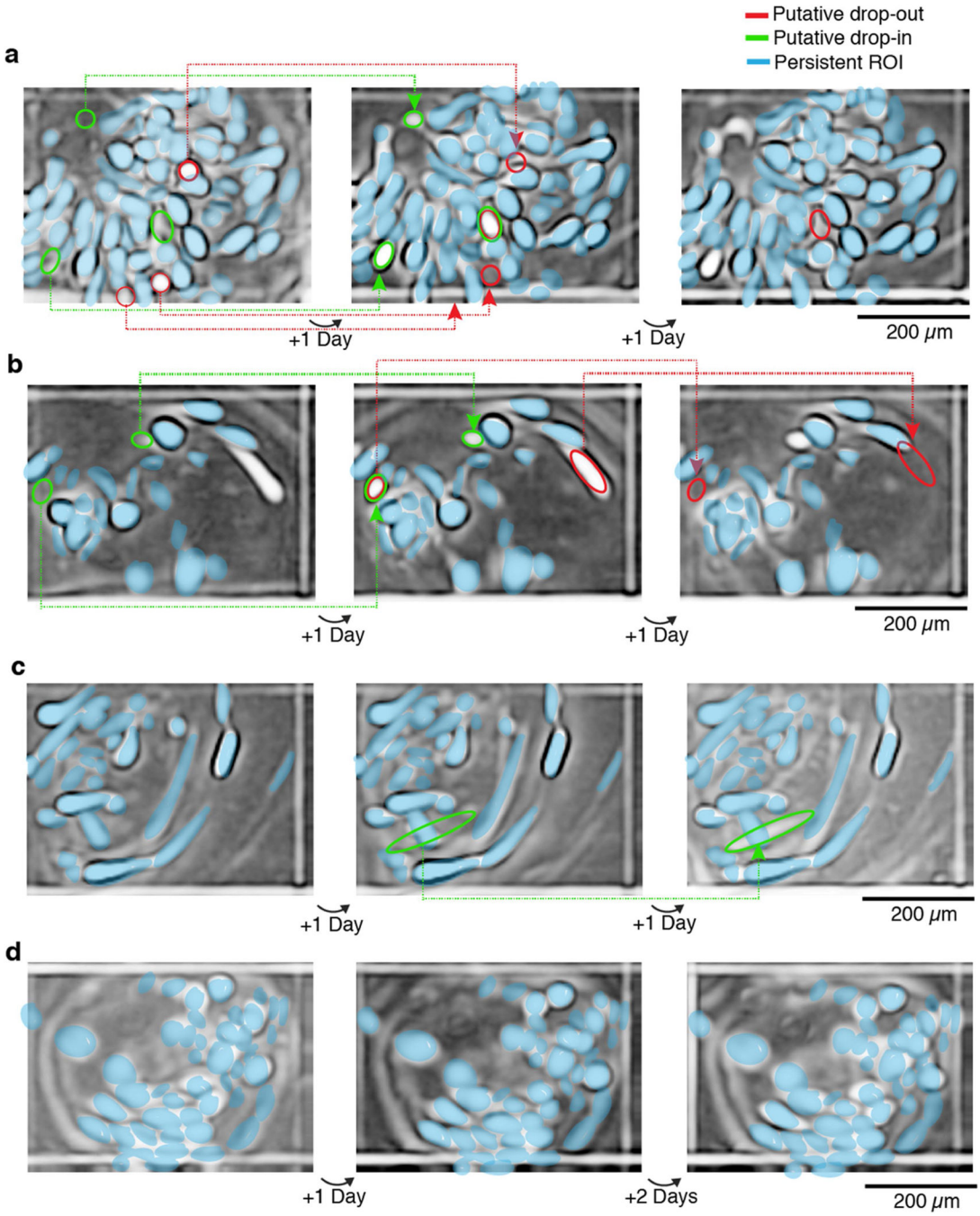

Extended Data Fig. 7 |. Examples of abrupt, possibly biologically-driven, changes in neural participation over days.

Maximum intensity projections of adjacent flight sessions that show several compelling examples of sharp in focus ROIs that could be unambiguously identified on one day but are clearly absent in the proceeding or following imaging session. Several of these examples are less likely to be a result of a slow change in imaging plane across days, which explains the majority of our tracking loss (that is, a slow change of ROI sharpness and intensity over consecutive sessions, as may be seen in some panels). Examples of abrupt changes in neural participation are sparse; panels **a–d** show different examples with panel **a** being the most

Author Manuscript Author Manuscript Author Manuscript Author Manuscript

obvious example found in our data set. Blue markers identify ROIs that are easily tracked on adjacent sessions. Red circles indicate an ROI that putatively 'drops-out' and green circles indicate an ROI that putatively 'drops-in.' Note that this phenomenon is uncommon and shown here to demonstrate the conservative approach: only 2.6% of clearly isolated ROIs identified on any given day show this effect (Methods).

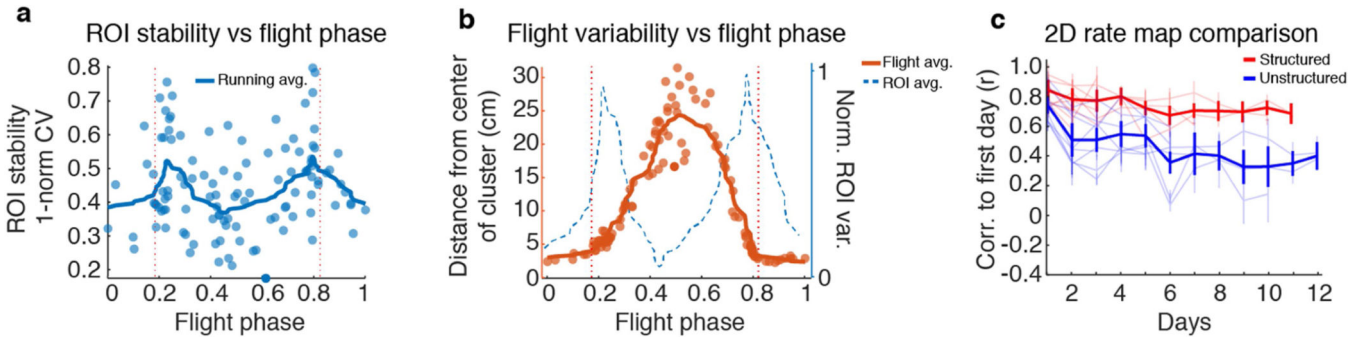

Extended Data Fig. 8 |. ROI tuning stability and flight consistency.

a, Flight-to-flight consistency varies along the phase of flight. Displayed are all ROIs tuned to the flight path shown in Fig. 3a, b. Each point represents a significantly tuned ROI's stability (that is, one minus the normalized coefficient of variation (CV)) at the flight phase it is tuned to (determined by the peak of the mean flight-aligned deconvolved activity trace). Red dotted lines indicate takeoff and landing times. The solid blue line is the running average of all points. **b**, Flight variability as a function of flight phase, sampled on the same interval as in **a**. Flight variability was highest in the middle of the flight and lowest during the takeoff and landing. The left *y*-axis units are the mean Euclidean distance of all individual flights from the centre of the mean flight path. The blue dotted line is the same as the blue solid line from **a**, normalized from 0–1 (right *y*-axis). **c**, More structured behaviour in freely flying bats results in the estimation of a more stable CA1 hippocampal responses over days. Longitudinal stability of hippocampal neural responses when considering either the most common structured flight path (that is, the flight path comprised of the largest number of flights, in red) and all non-repeated (that is, unstructured) flights in the same session (in blue) for $n = 7$ bats. Correlation is computed for 2D rate-maps relative to the first day of the experiment. Thin lines are different bats/flight paths and thick lines are the average across animals. Error bars represent 95% confidence intervals of the mean.

Author Manuscript Author Manuscript Author Manuscript Author Manuscript

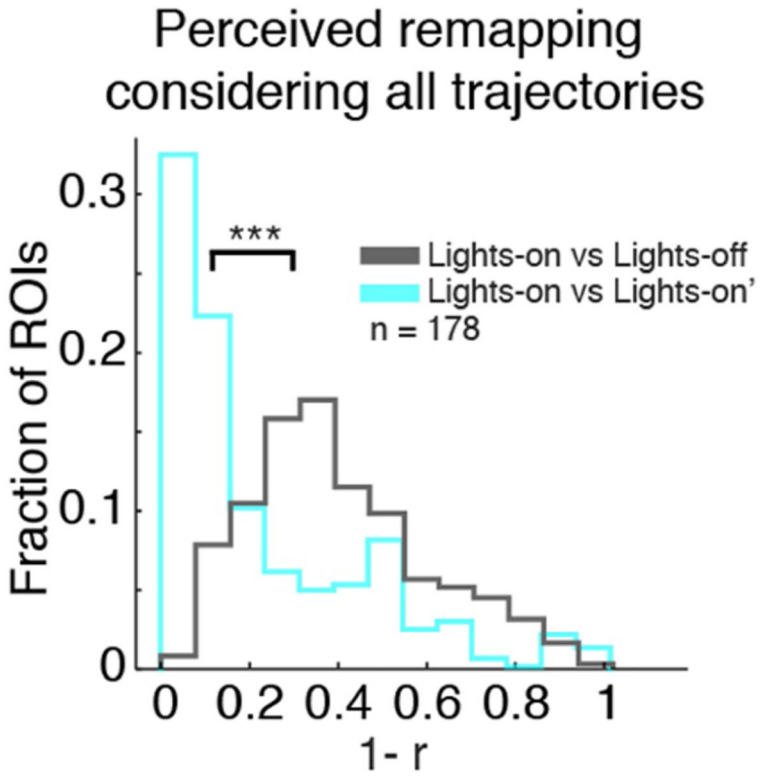

Extended Data Fig. 9 |. Perceived sensory-based remapping when considering all flight trajectories before controlling for flight behaviour variability across lights-on and lights-off conditions.

Shown is the distribution of 2D rate map correlation scores for all ROIs when considering all flight paths between either the two lights-on sessions (teal) or lights-on versus lights-off conditions (grey). These distributions are significantly different (n = 178 ROIs, $P = 7.04 \times 10^{-55}$, two-tailed Wilcoxon rank sum test). *** $P < 0.0001$.

Author Manuscript Author Manuscript Author Manuscript Author Manuscript

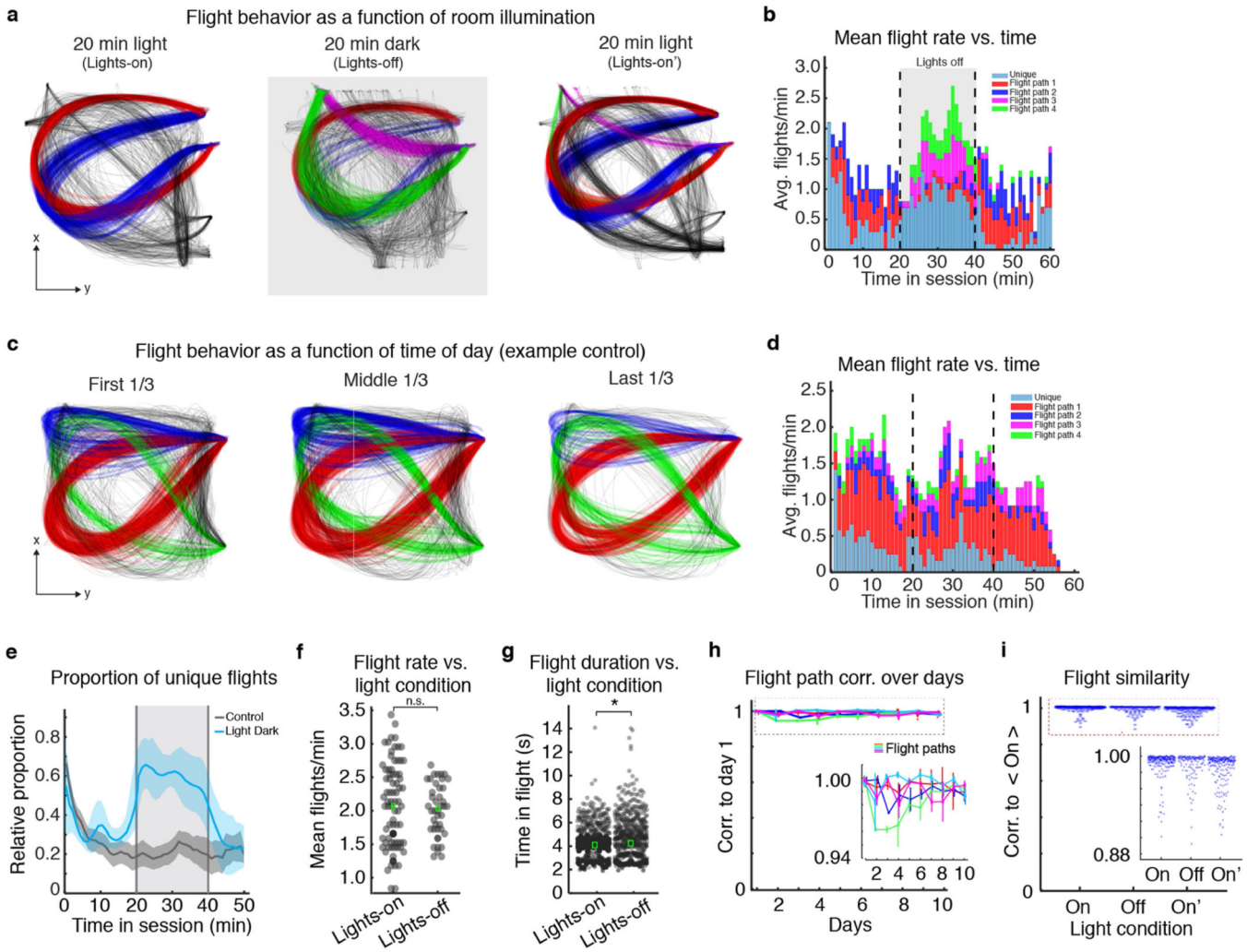

Extended Data Fig. 10 |. Similarities and differences in flight behaviour between the lights-on vs. lights-off cue conditions.

a, Aggregated flight paths that occurred across 10 consecutive days of experiments for one example bat, divided into successive lights-on, lights-off and lights-on′ periods (ordered from left to right). Coloured are the four most common flight paths. The red and blue flight paths occurred predominantly in lights-on and lights-on′ sessions. The green and magenta paths occurred predominantly in the lights-off condition. **b**, Distribution of the occurrence of the four most prevalent flight paths, coloured according to **a**, during different phases of the experiment across lights-on and lights-off sessions. Flight preference changed dramatically during each period. **c**, Aggregated flight paths across ten consecutive days for one representative bat divided into chronological thirds of each session where light levels were held constant. Shown are the three most common flight paths in red, blue and green. **d**, Distribution of the occurrence of the four most prevalent flight paths (colours) during different phases of the experiment across each third of ten sessions. **e**, Proportion of unique (that is, unstructured) flight paths increase on average in the lights-off cue condition (dark) compared to when the lights are kept on for the duration of the session. The blue line indicates the mean relative proportion of unique flights flown in the lights-on/off

Author Manuscript Author Manuscript Author Manuscript Author Manuscript

experiment. The dark grey line is the mean proportion of unstructured flights for bats where the light is kept on for the duration of the experiment. Shading for both plots represent 95% confidence intervals of the mean. **f**, The mean number of flights per minute is not significantly different in the light or dark conditions ($P > 0.05$ two-tailed Wilcoxon rank sum test, $n = 80$ and 40 binned minutes in the lights-on and lights-off periods respectively). Points are horizontally jittered for ease of visualization. **g**, Flight duration as function of cue condition. Flight duration is significantly longer in the lights-off condition, ($P = 0.0038$, two-tailed Wilcoxon rank sum test) although the effect size is small (that is, the distributions are highly overlapping; $n = 1{,}567$ and 746 flights in the lights-on and lights-off periods respectively). Points are horizontally jittered for ease of visualization. **h**, **i**, Across-day and across-condition behavioural stability for the lights-on versus lights-off experiments. **h**, Average correlation of repeated paths relative to day one for each bat ($n = 5$ flight paths). Each colour indicates a different flight path. Bars indicate 95% confidence intervals of the mean correlation on each day. **i**, Correlation values of shared flights to the mean of their flight path in the first lights-on period. Flights along the same path were not significantly different between the light and dark cue condition ($P = 0.21$ two-tailed Wilcoxon rank sum test, $n = 268$, 150, 267 flights for lights-on, lights-off and lights-on conditions, respectively). Points are horizontally jittered for ease of visualization. * $P < 0.01$.

Supplementary Material

Refer to Web version on PubMed Central for supplementary material.

Acknowledgements

We thank the members of the Yartsev laboratory and D. Foster laboratory for discussion and comments; E. Azim, B. Styr, J. Widloski and K. Qi for reading and comments on the manuscript; P. Golshani; T. Shuman, D. Cai and G. Blair for initial training on calcium imaging surgical techniques; N. Doston and D. Genzel for assistance with the experimental set-up; V. Shvareva and A. Rakuljic for help with histology; H. Aaron, F. Ives and staff at the CRL Molecular Imaging Center for assistance with the use of core imaging facilities; Y. Minton and L. Loomis for experimental room maintenance and animal care; G. Lawson, K. Jensen, J. Frohlich and the staff of the Office of Laboratory Animal Care for support with animal husbandry and care. This research was supported by the New York Stem Cell Foundation (NYSCF-R-NI40), Air Force Office of Scientific Research (FA9550-17-1-0412), the Packard Fellowship (2017-66825), National Institute of Neurological Disorders and Stroke (R01NS118422-01), the Valle Foundation (VS-2020-34), The Office of Naval Research (N00014-21-1-2063), the Searle Scholars Program (SSP-2016-1412) (to M.M.Y.) and the National Science Foundation Graduate Research Fellowship (to T.A.S).

References

1. O'Keefe J & Dostrovsky J. The hippocampus as a spatial map. Preliminary evidence from unit activity in the freely-moving rat. Brain Res. 34, 171–175 (1971). [PubMed: 5124915]
2. Moser EI, Moser M-B & McNaughton BL Spatial representation in the hippocampal formation: a history. Nat. Neurosci 20, 1448–1464 (2017). [PubMed: 29073644]
3. Geva-Sagiv M, Las L, Yovel Y. & Ulanovsky N. Spatial cognition in bats and rats: from sensory acquisition to multiscale maps and navigation. Nat. Rev. Neurosci 16, 94–108 (2015). [PubMed: 25601780]
4. Etienne AS et al. Navigation through vector addition. Nature 396, 161–164 (1998). [PubMed: 9823894]
5. Harten L, Katz A, Goldshtein A, Handel M. & Yovel Y. The ontogeny of a mammalian cognitive map in the real world. Science 369, 194–197 (2020). [PubMed: 32647001]
6. Toledo S. et al. Cognitive map-based navigation in wild bats revealed by a new high-throughput tracking system. Science 369, 188–193 (2020). [PubMed: 32647000]

Author Manuscript Author Manuscript Author Manuscript Author Manuscript

7. Ziv Y. et al. Long-term dynamics of CA1 hippocampal place codes. Nat. Neurosci 16, 264–266 (2013). [PubMed: 23396101]
8. Rubin A, Geva N, Sheintuch L. & Ziv Y. Hippocampal ensemble dynamics timestamp events in long-term memory. eLife 4, e12247 (2015). [PubMed: 26682652]
9. Gonzalez WG, Zhang H, Harutyunyan A. & Lois C. Persistence of neuronal representations through time and damage in the hippocampus. Science 365, 821–825 (2019). [PubMed: 31439798]
10. Mankin EA, Diehl GW, Sparks FT, Leutgeb S. & Leutgeb JK Hippocampal CA2 activity patterns change over time to a larger extent than between spatial contexts. Neuron 85, 190–201 (2015). [PubMed: 25569350]
11. Thompson LT & Best PJ Long-term stability of the place-field activity of single units recorded from the dorsal hippocampus of freely behaving rats. Brain Res. 509, 299–308 (1990). [PubMed: 2322825]
12. Hainmueller T. & Bartos M. Parallel emergence of stable and dynamic memory engrams in the hippocampus. Nature 558, 292–296 (2018). [PubMed: 29875406]
13. Moser EI, Kropff E. & Moser M-B Place cells, grid cells, and the brain's spatial representation system. Annu. Rev. Neurosci. 31, 69–89 (2008). [PubMed: 18284371]
14. Payne HL, Lynch GF & Aronov D. Neural representations of space in the hippocampus of a food-caching bird. Science 373, 343–348 (2021). [PubMed: 34437154]
15. O'Keefe J. & Nadel L. The Hippocampus as a Cognitive Map (Clarendon Press, Oxford Univ. Press, 1978).
16. Yartsev MM & Ulanovsky N. Representation of three-dimensional space in the hippocampus of flying bats. Science 340, 367–372 (2013). [PubMed: 23599496]
17. Wohlgemuth MJ, Yu C. & Moss CF 3D hippocampal place field dynamics in free-flying echolocating bats. Front. Cell. Neurosci. 12, 270 (2018). [PubMed: 30190673]
18. Tolman EC Cognitive maps in rats and men. Psychol. Rev 55, 189–208 (1948). [PubMed: 18870876]
19. Tsoar A. et al. Large-scale navigational map in a mammal. Proc. Natl Acad. Sci. USA 108, E718–E724 (2011). [PubMed: 21844350]
20. Muller R, Kubie J. & Ranck J. Spatial firing patterns of hippocampal complex-spike cells in a fixed environment. J. Neurosci 7, 1935–1950 (1987). [PubMed: 3612225]
21. Lütcke H, Margolis DJ & Helmchen F. Steady or changing? Long-term monitoring of neuronal population activity. Trends Neurosci. 36, 375–384 (2013). [PubMed: 23608298]
22. Clopath C, Bonhoeffer T, Hübener M. & Rose T. Variance and invariance of neuronal long-term representations. Philos. Trans. R. Soc. B 372, 20160161 (2017).
23. Levy SJ, Kinsky NR, Mau W, Sullivan DW & Hasselmo ME Hippocampal spatial memory representations in mice are heterogeneously stable. Hippocampus 31, 244–260 (2021). [PubMed: 33098619]
24. Kinsky NR et al. Trajectory-modulated hippocampal neurons persist throughout memory-guided navigation. Nat. Commun. 11, 2443 (2020). [PubMed: 32415083]
25. Liberti WA, Perkins LN, Leman DP & Gardner TJ An open source, wireless capable miniature microscope system. J. Neural Eng 14, 045001 (2017). [PubMed: 28514229]
26. Genzel D. & Yartsev MM The fully automated bat (FAB) flight room: a human-free environment for studying navigation in flying bats and its initial application to the retrosplenial cortex. J. Neurosci. Methods 348, 108970 (2021). [PubMed: 33065152]
27. Dotson NM & Yartsev MM Nonlocal spatiotemporal representation in the hippocampus of freely flying bats. Science 373, 242–247 (2021). [PubMed: 34244418]
28. Sarel A, Finkelstein A, Las L. & Ulanovsky N. Vectorial representation of spatial goals in the hippocampus of bats. Science 355, 176–180 (2017). [PubMed: 28082589]
29. Mallory CS & Giocomo LM Heterogeneity in hippocampal place coding. Curr. Opin. Neurobiol 49, 158–167 (2018). [PubMed: 29522977]
30. McNaughton BL, Barnes CA & O'Keefe J. The contributions of position, direction, and velocity to single unit activity in the hippocampus of freely-moving rats. Exp. Brain Res 52, 41–49 (1983). [PubMed: 6628596]

Author Manuscript Author Manuscript Author Manuscript Author Manuscript

31. Wood ER, Dudchenko PA, Robitsek RJ & Eichenbaum H. Hippocampal neurons encode information about different types of memory episodes occurring in the same location. Neuron 27, 623–633 (2000). [PubMed: 11055443]
32. Rubin A, Yartsev MM & Ulanovsky N. Encoding of head direction by hippocampal place cells in bats. J. Neurosci 34, 1067–1080 (2014). [PubMed: 24431464]
33. Geva-Sagiv M, Romani S, Las L. & Ulanovsky N. Hippocampal global remapping for different sensory modalities in flying bats. Nat. Neurosci 19, 952–958 (2016). [PubMed: 27239936]
34. Kentros CG, Agnihotri NT, Streater S, Hawkins RD & Kandel ER Increased attention to spatial context increases both place field stability and spatial memory. Neuron 42, 283–295 (2004). [PubMed: 15091343]
35. Muzzio IA et al. Attention enhances the retrieval and stability of visuospatial and olfactory representations in the dorsal hippocampus. PLoS Biol. 7, e1000140 (2009). [PubMed: 19564903]
36. Dupret D, O'Neill J, Pleydell-Bouverie B. & Csicsvari J. The reorganization and reactivation of hippocampal maps predict spatial memory performance. Nat. Neurosci 13, 995–1002 (2010). [PubMed: 20639874]
37. Tchernichovski O, Benjamini Y. & Golani I. The dynamics of long-term exploration in the rat. Part I. A phase-plane analysis of the relationship between location and velocity. Biol. Cybern. 78, 423–432 (1998). [PubMed: 9711816]
38. Yartsev MM The emperor's new wardrobe: rebalancing diversity of animal models in neuroscience research. Science 358, 466–469 (2017). [PubMed: 29074765]
39. Krakauer JW, Ghazanfar AA, Gomez-Marin A, MacIver MA & Poeppel D. Neuroscience needs behavior: correcting a reductionist bias. Neuron 93, 480–490 (2017). [PubMed: 28182904]
40. Yovel Y, Geva-Sagiv M. & Ulanovsky N. Click-based echolocation in bats: not so primitive after all. J. Comp. Physiol. A 197, 515–530 (2011).
41. Holland RA, Waters DA & Rayner JMV Echolocation signal structure in the Megachiropteran bat *Rousettus aegyptiacus* Geoffroy 1810. J. Exp. Biol 207, 4361–4369 (2004). [PubMed: 15557022]
42. Lee W-J et al. Tongue-driven sonar beam steering by a lingual-echolocating fruit bat. PLoS Biol. 15, e2003148 (2017). [PubMed: 29244805]
43. Danilovich S. & Yovel Y. Integrating vision and echolocation for navigation and perception in bats. Sci. Adv 5, eaaw6503 (2019).
44. El-Mansi AA, Al-Kahtani MA, Al-Sayyad KM, Ahmed EA & Gad AR Visual adaptability and retinal characterization of the Egyptian fruit bat (*Rousettus aegyptiacus*, Pteropodidae): new insights into photoreceptors spatial distribution and melanosomal activity. Micron 137, 102897 (2020).
45. Ghosh KK et al. Miniaturized integration of a fluorescence microscope. Nat. Methods 8, 871–878 (2011). [PubMed: 21909102]
46. Groot AD, Genderen RMV, Coppens J, Zeeuw ID & Hoogland TM NINscope: a versatile miniscope for multi-region circuit investigations. eLife 9, e49987 (2019).
47. Shuman T. et al. Breakdown of spatial coding and interneuron synchronization in epileptic mice. Nat. Neurosci 23, 229–238 (2020). [PubMed: 31907437]
48. Cai DJ et al. A shared neural ensemble links distinct contextual memories encoded close in time. Nature 534, 115–118 (2016). [PubMed: 27251287]
49. Kügler S, Kilic E. & Bähr M. Human synapsin 1 gene promoter confers highly neuron-specific long-term transgene expression from an adenoviral vector in the adult rat brain depending on the transduced area. Gene Ther. 10, 337–347 (2003). [PubMed: 12595892]
50. Barchi JR, Knowles JM & Simmons JA Spatial memory and stereotypy of flight paths by big brown bats in cluttered surroundings. J. Exp. Biol 216, 1053–1063 (2013). [PubMed: 23447667]
51. Guizar-Sicairos M, Thurman ST & Fienup JR Efficient subpixel image registration algorithms. Opt. Lett 33, 156–158 (2008). [PubMed: 18197224]
52. Huang L. et al. Relationship between simultaneously recorded spiking activity and fluorescence signal in GCaMP6transgenic mice. eLife 10, e51675 (2021). [PubMed: 33683198]
53. Sheintuch L. et al. Tracking the same neurons across multiple days in $Ca2^{+}$ imaging data. Cell Rep. 21, 1102–1115 (2017). [PubMed: 29069591]

Author Manuscript Author Manuscript Author Manuscript Author Manuscript

54. Zhou P. et al. Efficient and accurate extraction of in vivo calcium signals from microendoscopic video data. eLife 7, e28728 (2018). [PubMed: 29469809]

55. Pnevmatikakis EA et al. Simultaneous denoising, deconvolution, and demixing of calcium imaging data. Neuron 89, 285–299 (2015).

56. Skaggs WE, McNaughton BL, Wilson MA & Gothard KM An information-theoretic approach to deciphering the hippocampal code. In Adv. Neural Inf. Process. Syst. 5 (eds Hanson SJ, Cowan JD & Giles CL) 1030–1037 (Morgan Kaufman, San Mateo, 1993).

57. Zhang K, Ginzburg I, McNaughton BL & Sejnowski TJ Interpreting neuronal population activity by reconstruction: unified framework with application to hippocampal place cells. J. Neurophysiol 79, 1017–1044 (1998). [PubMed: 9463459]

58. Carpenter J, Blackstad J, Dunn B, Moser EI & Moser M-B Egocentric tuning in hippocampal neurons: using simulations to estimate misclassification rates. In Proc. Soc. Neurosci P871.08 (2021).

Author Manuscript Author Manuscript Author Manuscript Author Manuscript

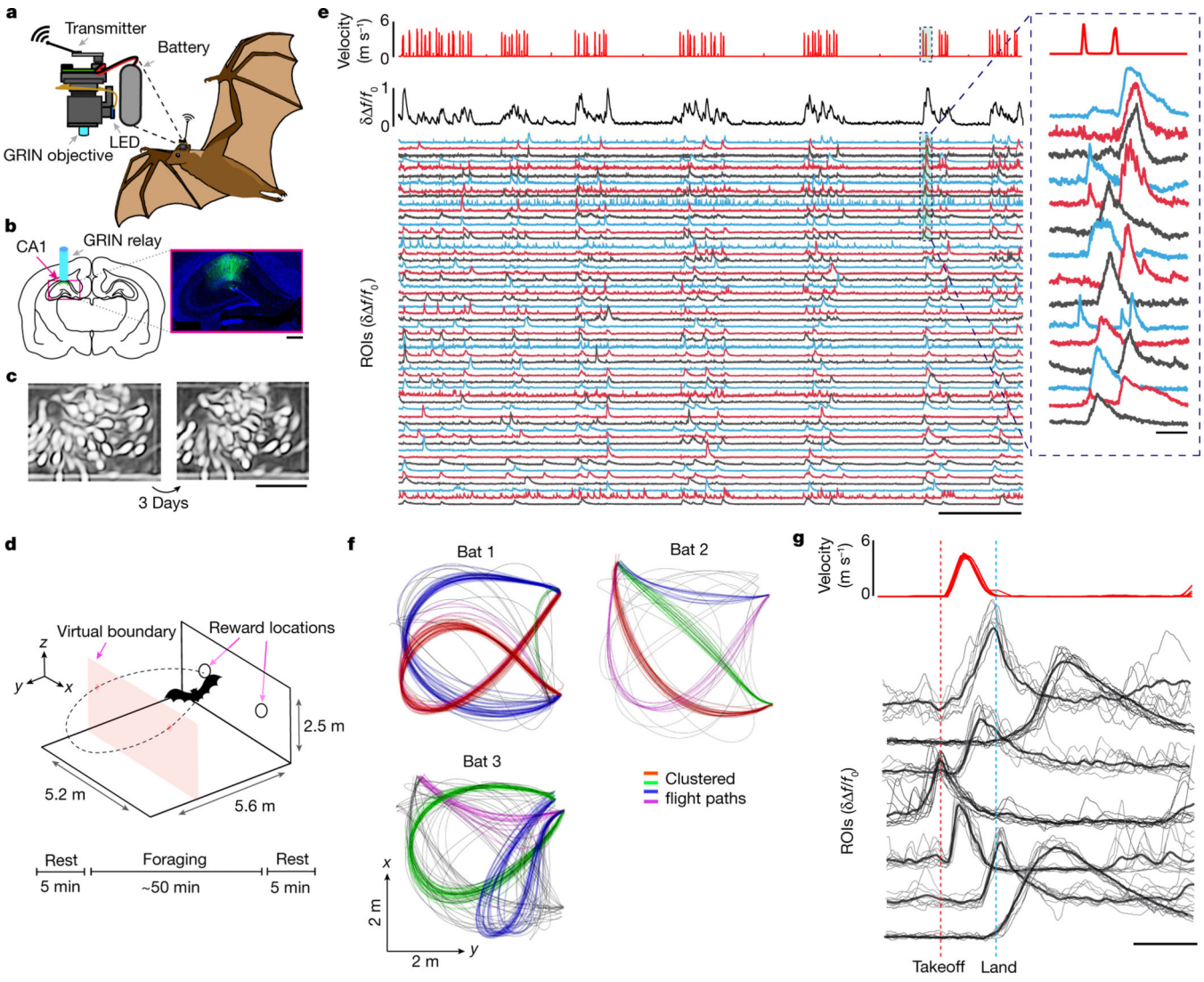

Fig. 1 |. Wireless calcium imaging and spatial movement patterns in freely flying bats.

a, Schematic of a bat carrying a wireless miniature microscope system during flight. **b**, A GRIN lens was implanted above dorsal CA1. Inset, coronal section of the hippocampus with GCaMP6f (green) and nuclear (4′,6-diamidino-2-phenylindole (DAPI), blue) staining. Scale bar, 500 μm. **c**, Two example maximum intensity $\Delta f/f_0$ projections from one bat, separated by 3 days. Scale bar, 200 μm. **d**, Flight room schematic and experimental paradigm. Two feeders on one wall dispensed a pureed fruit reward after landing if a virtual boundary was crossed during the flight. Bottom, experimental session timeline. **e**, Experimental data from the same animal shown in **c**. Top, bat velocity (m s^{-1}). Middle, the mean calcium activity of all ROIs. Units are normalized (δ) $\Delta f/f_0$. Bottom: fluorescent time series of 54 ROIs over the entire foraging session. Inset: magnification of calcium activity during two flights. Scale bars, 5 min (left) and 10 s (right). **f**, Representative flight paths (top view, *xy* projection) across a single session from three different example bats showing the diversity of structured routes taken by each animal. Flights for each bat are clustered by similar paths (colours). **g**, Neural responses aligned to flight activity. Top, bat velocity (m s^{-1}) for 15 flights along

Author Manuscript Author Manuscript Author Manuscript Author Manuscript

the same path. Bottom, calcium traces from seven simultaneously recorded ROIs for flights along the same path in a single bat, aligned to flight takeoff. The mean across flights for each ROI is shown in black. Individual flights are shown in grey. Scale bar, 3 s.

Author Manuscript
Author Manuscript
Author Manuscript
Author Manuscript

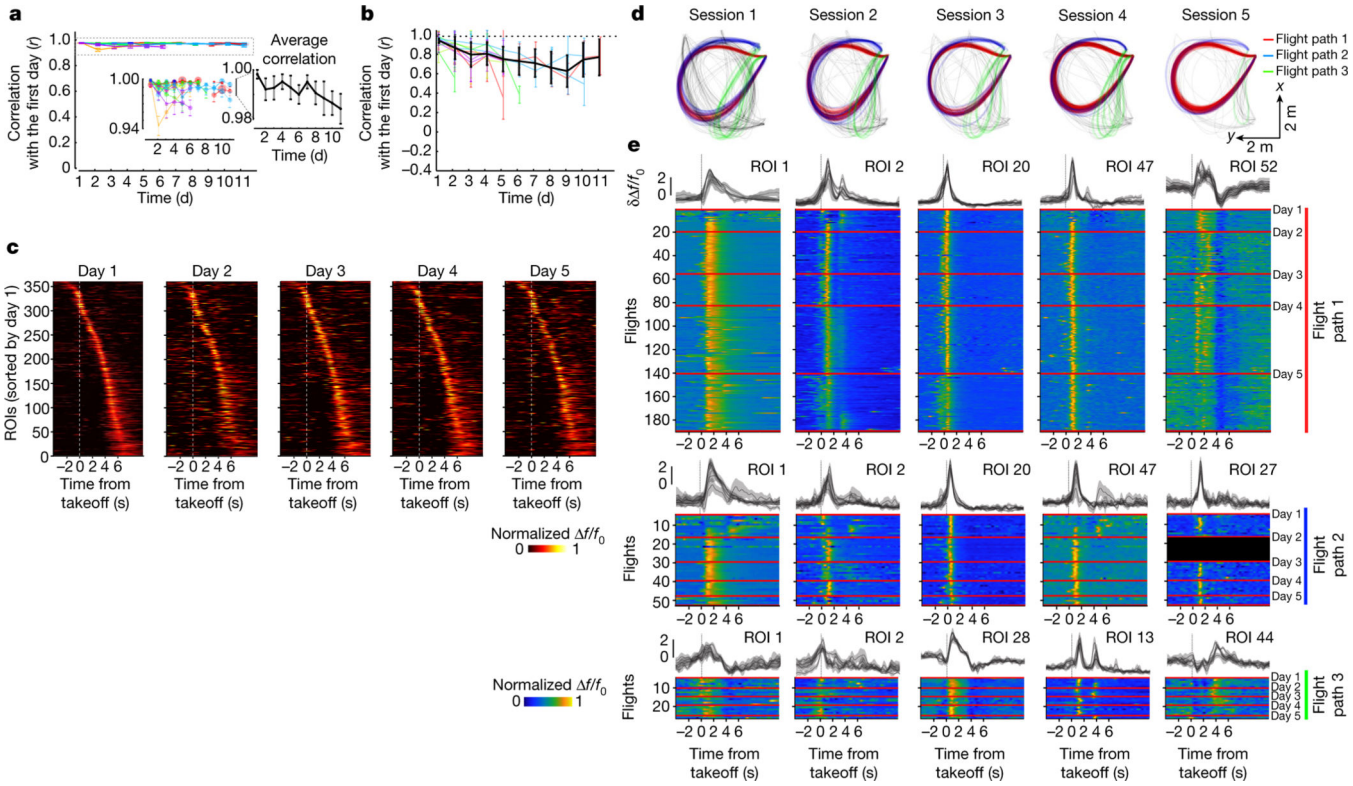

Fig. 2 |. Neural tuning for stable flight paths persists across days.

a, The average correlation of flights from the same cluster across different day lags, computed relative to the first day for each bat (different colours). The marker size corresponds to the relative number of flights in a session. Inset: magnification of the higher correlation values. Data are mean ± 99% confidence interval across $n = 7$ bats. **b**, The average correlation of neural tuning to the first day across all spatial firing fields and across different day lags for each bat; each colour indicates a different bat. Data are mean ± 99% confidence interval across $n = 7$ bats. **c**, Trial-averaged activity from all significantly flight-tuned neurons from all of the animals that could be tracked over a 5-day interval, sorted by peak activity on day 1. The same sorting was maintained for all subsequent days. **d**, Example flight patterns across five sessions performed over six days (with a one-day break between the fourth and fifth sessions). Common flight paths are coloured red, green and blue. **e**, Example ROIs (normalized $\Delta f/f_0$) aligned to takeoff (vertical grey dotted line) of the three most common flight paths. The x axis is extended relative to **c** to show that the calcium signals return to the baseline. Top, activity trace for each day (grey). Data are mean ± s.d. Bottom, chronological trial-by-trial responses aligned to flights (different flight paths are separated from top to bottom). The red lines for each ROI separate different days. In ROI 27, the black area indicates that the ROI was not confidently identified for that session.

Author Manuscript Author Manuscript Author Manuscript Author Manuscript

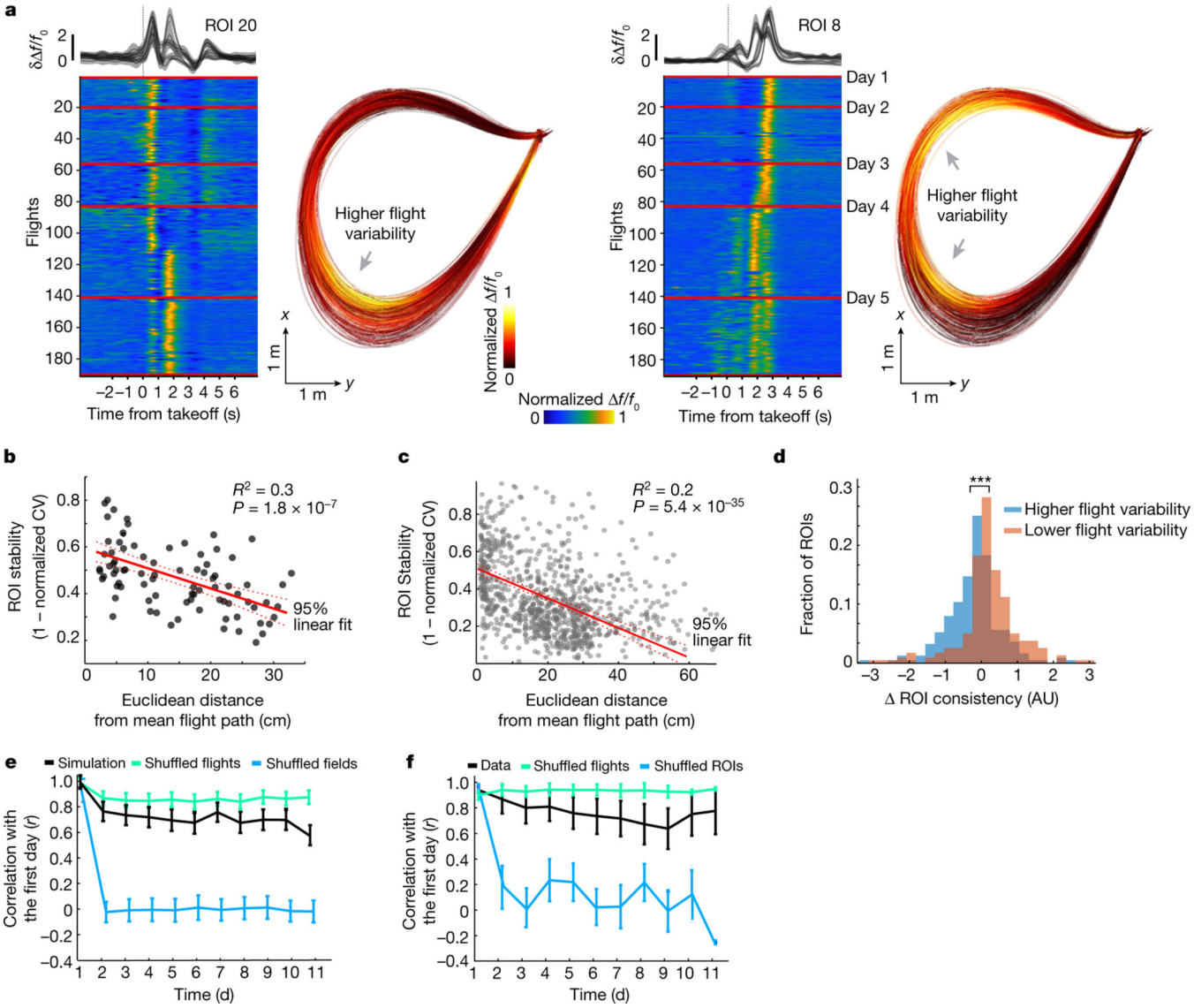

Fig. 3 |. Apparent changes in neural tuning can be explained by measurable changes in flight behaviour.

a, Two example ROIs with apparent unstable tuning. For each example, the average calcium responses in units of normalized $\Delta f/f_0$, aligned to takeoff (vertical grey dotted line) (top left); the chronological flight-by-flight responses (bottom left; the red lines indicate day transitions); and calcium $\Delta f/f_0$ superimposed as a heat map onto an *xy* projection of individual flight paths (right) are shown. Note that the neuron is active where there is increased flight variability (arrows). **b**, Correlation of ROI stability and flight variability (Methods) for the example bat shown in **a**, demonstrating that flight–flight variability is significantly correlated with the trial–trial variability seen in neural activity. **c**, Correlation of ROI stability and flight variability across all ROIs for the top three flight paths for all bats. **d**, Comparing flight-by-flight consistency for ROIs that are significantly tuned to more than one trajectory. ROI consistency is separated into two groups on the basis of flight variability: more variable flights are shown in blue and less variable flights are shown in orange.

Author Manuscript Author Manuscript Author Manuscript Author Manuscript

Note that there is a significant difference in the distribution of flight-by-flight consistency with lower flight variability corresponding to higher neural consistency. **e**, Average ROI correlation to day one across different lags (days) for simulated stable firing fields in black, shuffling ROI identity (blue) and shuffling flight order to eliminate behavioural drift (green). **f**, The same as in **e**, but with the mean correlation of empirically recorded Ca^{2+} data for all ROIs across different lags for each bat in black, shuffling ROI identity (blue) and shuffling flight order to eliminate behavioural drift (green). For **e** and **f**, data are mean ± 99% confidence intervals across $n = 7$ bats. ***$P < 0.0001$.

Author Manuscript Author Manuscript Author Manuscript Author Manuscript

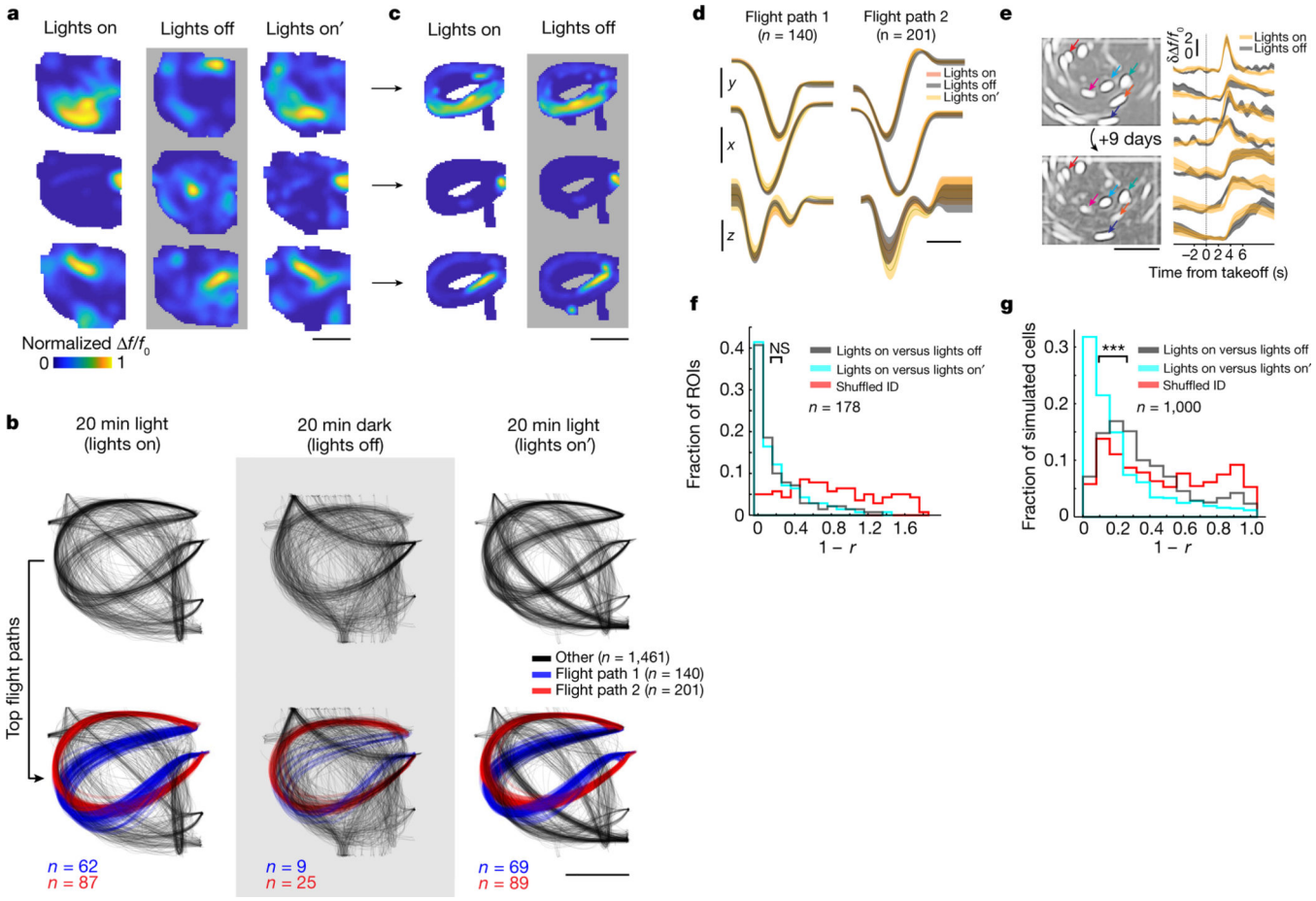

Fig. 4 |. Neural tuning persists despite a change in sensory context.

a, 2D firing maps for three example ROIs in lights on versus lights off cue conditions when considering all flights in each condition. Scale bars, 2 m. **b**, All flight paths that occurred across 10 consecutive days for one example bat, divided into successive lights on, lights off and lights on′ periods (ordered from left to right, respectively) (top). Bottom, two routes that persisted across all conditions, clustered in red and blue. The number of flights for each route in each condition is indicated. Scale bar, 2 m. **c**, 2D firing maps for the same three ROIs shown in **a**, considering only the same spatial trajectories exhibited in both conditions. **d**, Change in *x*, *y* and *z* position over time and across lighting conditions for the two conserved routes taken in the lights on and lights off periods shown in **b**. The shading represents 2 s.d. Scale bars, 100 cm (top left), 200 cm (middle left), 50 cm (bottom left) and 2 s (bottom right). **e**, Maximum intensity $\Delta f/f_0$ projection of the calcium activity in a single foraging session from one bat, separated by nine days, with a subset of tracked ROIs labelled with coloured arrows (left). Right, mean $\Delta f/f_0$ calcium responses aligned to the same path in the lights on (yellow) and lights off (grey) conditions. The shading indicates the s.d. Scale bar, 200 μm. **f**, The distribution of ROI tuning changes of 2D firing rate maps across the lights on versus lights on′ conditions (teal), and the lights on versus lights off (grey) conditions are not significantly different. $n = 178$ fields. Statistical analysis was performed using a two-tailed Wilcoxon rank-sum test; $P > 0.05$. **g**, The correlation of 2D firing rate maps of simulated stable tuning fields is significantly different when comparing across the

Author Manuscript Author Manuscript Author Manuscript Author Manuscript

lights on versus lights on′ conditions (teal), and lights on versus lights off conditions (grey). Both are significantly different from shuffling the field identity (red). ***$P < 0.0001$. NS, not significant.